UNIVERSITY OF LEEDS

This is a repository copy of *Particle behavior in a turbulent pipe flow with a flat bed*.

White Rose Research Online URL for this paper:
https://eprints.whiterose.ac.uk/195821/

Version: Accepted Version

Article:
Liu, M, Zhao, Y, Yan, Y et al. (2 more authors) (2023) Particle behavior in a turbulent pipe flow with a flat bed. Particuology, 81. pp. 58-72. ISSN 1674-2001

https://doi.org/10.1016/j.partic.2022.12.016

© 2023 Chinese Society of Particuology and Institute of Process Engineering, Chinese Academy of Sciences. Published by Elsevier B.V. All rights reserved. This manuscript version is made available under the CC-BY-NC-ND 4.0 license http://creativecommons.org/licenses/by-nc-nd/4.0/.

Reuse
This article is distributed under the terms of the Creative Commons Attribution-NonCommercial-NoDerivs (CC BY-NC-ND) licence. This licence only allows you to download this work and share it with others as long as you credit the authors, but you can't change the article in any way or use it commercially. More information and the full terms of the licence here: https://creativecommons.org/licenses/

Takedown
If you consider content in White Rose Research Online to be in breach of UK law, please notify us by emailing eprints@whiterose.ac.uk including the URL of the record and the reason for the withdrawal request.

White Rose university consortium
Universities of Leeds, Sheffield & York

eprints@whiterose.ac.uk
https://eprints.whiterose.ac.uk/

Particle behavior in a turbulent pipe flow with a flat bed

Min Liu[1], Yanlin Zhao[1a)], Yudong Yan[1], Michael Fairweather[2] , Jun Yao[1]

[1] International Joint Laboratory on Clean Energy Science and Technology, Beijing Key Laboratory of Process Fluid Filtration and Separation, College of Mechanical and Transportation Engineering, China University of Petroleum-Beijing, Beijing 102249, People's Republic of China

[2] School of Chemical and Process Engineering, University of Leeds, Leeds, LS2 9JT, UK

Submitted for publication in

PARTICUOLOGY

July 2022

[a)]**Author to whom correspondence should be addressed**: ylzhao@cup.edu.cn

Prof. Jun Yao, International Joint Laboratory on Clean Energy Science and Technology, College of Mechanical and Transportation Engineering, China University of Petroleum-Beijing, Beijing 102249, People's Republic of China

Telephone: +86 (0) 10 89733685; Facsimile: +86 (0) 10 89733658; Email address: ylzhao@cup.edu.cn

ABSTRACT

Particle behavior in a turbulent flow in a circular pipe with a bed height $h = 0.5R$, is studied at $Re_b = 40{,}000$ and for two sizes of particles ($5\mu m$ and $50\mu m$) using large eddy simulation, one-way coupled with a Lagrangian particle tracking technique. Turbulent secondary flows are found within the pipe, with the curved upper wall affecting the secondary flow formation giving rise to a pair of large upper vortices above two smaller vortices close to the pipe floor. The behavior of the two sizes of particle is found to be quite different. The 50μm particles deposit forming irregular elongated particle streaks close to the pipe floor, particularly at the center of the flow and the pipe corners due to the impact of the secondary flows. The deposition and resuspension rate of the 5μm particles is high near the center of the floor and at the pipe corners, while values for the 50μm particles are greatest near the corners. Near the curved upper wall of the pipe, the deposition rate of the 5μm particles increases in moving from the wall center to the corners, and is greater than for the larger particles due to the effects of the secondary flow. The maximum resuspension rate of the smaller particles occurs above the pipe corners, with the 50μm particles showing their highest resuspension rate above and at the corners of the pipe.

1. Introduction

As one of the most important transportation modes of fluid media such as oil, natural gas and fine chemicals, to name a few, pipelines with circular cross-section are ubiquitous in most industries. The fluid flow in a circular pipe is so common that it has been studied extensively, including, for example, turbulent single-phase flows (Cantwell, 2019; El Khoury et al., 2013; Peng et al., 2018) and particle-laden flows (Arolla & Desjardins, 2015). These and many other studies have greatly assisted the understanding of such flows and promoted the use of pipes in many industrial applications.

In order to focus on particle dispersion and interaction in multi-phase flows, and preclude distraction from secondary factors, gravity has often been ignored in studies of particle-laden flow in circular pipes, with the particle motion considered solely as a results of fluid action (Battista at al., 2019). However, in a long pipeline, for example, particles tend to deposit and settle at the bottom of the pipe under the action of gravity. The particles deposit gradually, ultimately forming a particle layer, or bed, at the bottom of the pipe which impacts the flow behavior and its properties. This situation is quite common in many industries, and is clearly undesirable given the consequences of pipe blockages, their impact on maintenance costs and the risk of increased erosion. Similarly, in natural gas pipelines that contain high sulfur content gases, chemical reaction can occur with the metal pipe walls, producing particles that again have the potential to settle at the bottom of the pipe (Sherik et al, 2008). Therefore, the study of flows in pipes with a flat bed is of significant practical interested.

Unlike in full pipes of circular cross-section, secondary flows are generated in turbulent flows in pipes with a flat bed because of the corner of the cross-section. It is known that secondary flows can be divided into two groups (Bradshaw, 1987), with one type found in turbulent flows in straight non-circular ducts. In these flows a net secondary flow of Prandtl's second kind occurs, with counter-rotating vortices present around the duct's corner bisectors, with four such pairs of vortices in the duct as a whole (Nikuradse, 1930; Prandtl, 1926). These secondary flows move from the duct center to its corners and then back to the center of the duct along the wall, transporting momentum together with other flow properties such as streamwise velocity (contours curving toward the corners) and turbulence kinetic energy. The velocity magnitude of the secondary flows is higher near the corners of the duct and on the angular bisectors in comparison with other areas of the flow, although the secondary flow is relatively weak in square ducts and only 1-3% of the mean streamwise velocity (Brundrett & Baines, 1964; Gavrilakis, 1992; Madabhushi & Vanka, 1991; Pirozzoli et al., 2018).

Similar to the pipe flow with a flat bed studied in this work, two pairs of corner vortices have been found in the cross-section of turbulent semi-circular pipe flows (Larsson et al., 2011; Liu et al., 2021a). Since there are only two corners in the semi-circular pipe, the number of corner vortices is half of that found in the square duct (Yao & Fairweather, 2010, 2012; Zhao et al., 2018), with the curved wall of the pipe inhibiting the size of the vortices adjacent to that surface. Similar secondary flows have also been reported in laminar semi-circular pipe flows (El Hasadi et al., 2007), although in this case the heated walls meant that their formation was driven by buoyancy effects.

The turbulence field in a right-angled equilateral triangular duct with angles of 30° and 60° was also measured using hot-wire anemometry by Hurst and Rapley (1991), again demonstrating the presence of counter-rotating vortices about the corner bisectors, with the secondary motions generated by flow over a streamwise external corner measured by Moinuddin et al. (2004) and over a right-angled plane by Nagata et al. (2010). Counter-rotating vortices of Prandtl's second kind have also been observed in DNS simulations of elliptical ducts (Nikitin & Yakhot, 2005), hexagonal ducts (Marin et al., 2016) and square ducts with rounded corners (Vidal et al., 2017).

Although secondary flows of the second kind are relatively weak, they affect particle behavior in the cross-sectional plane orthogonal to the flow direction (Yao & Fairweather, 2010, 2012; Zhao et al., 2018). For example, particles dispersed in turbulent square duct flows tend to be transported by the secondary flows, with their lateral mixing enhanced, for low inertia particles at least (Sharma & Phares, 2006). If gravity is considered, high inertia particles affect the flow and cause the upper secondary motions to move down towards the duct center due to particle sedimentation, destroying the symmetry between the upper and lower secondary flows that occur in the square duct (Lin et al., 2017). If the particle density is the same as that of the fluid, the addition of particles enhances the secondary flow motion and causes their circulation centers to approach the center of the duct (Lin et al., 2017). If electrostatic forces between the particles are considered, they have a significant influence on particle behavior, dominating the secondary flow and preventing particles from moving away from the duct walls (Grosshans et al., 2021). In addition, the lift force acting on the

particles caused by the streamwise velocity gradient is found to be much less than that attributable to the velocity gradient of the cross-flow (Winkler & Rani, 2009).

Particle distributions in turbulent flows in geometries other than square ducts have also been investigated. For example, in a rectangular cross-section duct with an aspect ratio of 3, the highest particle concentrations in the viscous sub-layer were found near the duct corners, in contrast to flows in a square duct where the highest concentration in the sub-layer was found at the center plane (Noorani et al., 2016), with Voronoi analysis demonstrating that particle clustering occurs due to near-wall coherent flow structures and associated secondary flows (Rabencov & van Hout, 2015). Particle distributions in circular pipes with variable bed height have also been reported where, for larger particles, the presence of a stationary flat bed was found not to influence the particle deposition rate, whereas for smaller particles an increased bed height led to a decrease in the particle mean displacement from the pipe walls with time (Adams et al., 2011). The latter are the only predictions of particle distributions in circular pipes with a flat bed available in the literature and, unlike in the present work, were obtained using a Reynolds-averaged Navier Stokes approach.

In terms of simulation methods, large eddy simulation (LES) has been widely used, together with Lagrangian particle tracking (LPT), in predicting a broad range of particle-laden flows (Almeida & Jaberi, 2008; Dritselis & Vlachos, 2011; Gallen et al., 2019; Kasper et al., 2019; Kriebitzsch & Richter, 2020; Luo et al. 2004; Pakseresht & Apte, 2019; Wang & Squires, 1996; Yao & Fairweather, 2010, 2012; Zhao et al., 2018). It should be noted that sub-grid scale turbulence cannot be obtained using LES, and the

influence of vortices at such scales on particles cannot be readily predicted. However, provided the LES is sufficiently resolved, and the sub-grid scale turbulence kinetic energy may be ignored, then the influence of the sub-grid model on the point particle assumption is negligible (Fröhlich et al., 2018).

A method to simulate the sedimentation process in a pipe is not considered in this work since the prime focus is on the impact of the secondary flows, caused by a simulated particle bed, have on particle behavior. There are also considerable difficulties associated with models of deposition and the resulting bedform. For example, under the action of gravity and inter-particle forces, four-way coupling (i.e. two-way coupling between the fluid flow and the particles, such that the fluid influences the particles and the particles influence the fluid, and collisions between particles) between the particles and the fluid flow will occur, with associated particle agglomeration. Additionally, bedforms in pipe flows can be categorised into five types (Rice et al., 2017): plane flat beds that do not vary with time; bedforms of regular period (time independent); time-dependent bedforms of increasing period; time dependent bedforms with unstable/cyclic period; and beds with no particle motion on the surface of the bed. Particle deposition, bed formation and evolution are therefore complex processes the prediction of which would entail high computational costs, particularly since the use of boundary resolving approaches for the particles would be required. In this work therefore, and given that flat beds that do not vary with time are one category of bedform, a simplified approach is adopted in which the lower regions of the pipe are assumed to be completely occupied by deposited particles that form a sediment bed

whose surface is assumed to be smooth. Clearly this still remains ideal, ignoring as it does the roughness of the bed surface, but such factors detract from the prime focus noted above. At this stage, only one height of sediment bed is considered. The impact of changing bed height on the flow field and particle behavior will be investigated further in the future. Nevertheless, the work described presents an original contribution in using high accuracy large eddy simulation, coupled to Lagrangian particle tracking, to study particle behavior in a turbulent flow in a circular pipe containing a flat bed, and more specifically in elucidating the influence of the turbulent secondary flows found within the pipe on that behavior.

2. Methodology

2.1 Large eddy simulation

LES with a top hat filter was used to simulate the flow field in the pipe with flat bed. The continuity and momentum equations of the filtered incompressible fluid flow are given as follows:

$$\frac{\partial \overline{u}_j}{\partial x_j} = 0 \tag{1}$$

$$\frac{\partial \overline{u}_i}{\partial t} + \frac{\partial \overline{u}_i \overline{u}_j}{\partial x_j} = -\frac{\partial \overline{p}/\rho}{\partial x_i} - \frac{\partial}{\partial x_j}(\overline{\sigma}_{ij} + \tau_{ij}), \tag{2}$$

where the superscript "‾" indicates the filtering operation. p, u_i and x_i are the pressure, velocity components, and position components of the fluid flow, respectively, and ρ is the fluid density. σ_{ij} is the kinematic viscous stress tensor and τ_{ij} is the sub-grid scale stress, defined as:

$$\bar{\sigma}_{ij} = -2\nu\bar{s}_{ij} \tag{3}$$

and $$\tau_{ij} = \overline{u_i u_j} - \bar{u}_i \bar{u}_j \tag{4}$$

where $$\bar{s}_{ij} = \frac{1}{2}\left(\frac{\partial \bar{u}_i}{\partial x_j} + \frac{\partial \bar{u}_j}{\partial x_i}\right). \tag{5}$$

The sub-grid scale stress tensor was computed using the dynamic version of the Smagorinsky model proposed by Piomelli and Liu (1995). The eddy viscosity model of Smagorinsky (1963) for this tensor linearly relates the anisotropic part of the tensor τ_{ij}^a to the filtered strain-rate tensor, $\bar{S}_{ij}$, via an eddy viscosity coefficient, $\mu_{sgs} = \rho\nu_{sgs}$, with νa length scale $\Delta = (\Delta_x\Delta_y\Delta_z)^{1/3}$ proportional the numerical grid spacing, hence:

$$\tau_{ij}^a = -2\nu_{sgs}\bar{S}_{ij} \tag{6}$$

where $$\nu_{sgs} = (C_s\bar{\Delta})^2 \,\|\bar{\mathbf{S}}\| \tag{7}$$

and $$\|\bar{\mathbf{S}}\| = \sqrt{2\bar{S}_{ij}\bar{S}_{ij}}\,. \tag{8}$$

Here, C_s is an adjustable parameter, the Smagorinsky constant, which needs to be specified. Previous studies have, however, demonstrated that model predictions are relatively insensitive to the value of C_s. In the present work, therefore, the approximate localised dynamic model of Piomelli and Liu (1995) was employed to determine C_s according to (Bini & Jones, 2008):

$$\left[C_s(\mathbf{x},t)\right]^2 = \frac{\left[\overline{(C_s^*)^2\alpha_{ij}} - L_{ij}^a\right]\overline{\bar{S}_{ij}}}{2\Delta_T^2\,\|\bar{\bar{\mathbf{S}}}\|\left(\overline{\bar{S}_{ij}} - \frac{\delta_{ij}}{3}\overline{\bar{S}_{kk}}\right)\overline{\bar{S}_{ij}}} \tag{9}$$

where $$\alpha_{ij} = 2\Delta^2\,\|\bar{\bar{\mathbf{S}}}\|\left(\bar{S}_{ij} - \frac{\delta_{ij}}{3}\bar{S}_{kk}\right) \tag{10}$$

and $$L_{ij} = \overline{\bar{u}_i\bar{u}_j} - \bar{\bar{u}}_i\bar{\bar{u}}_j\,, \tag{11}$$

and the superscript "–" indicates the application of a test filter of width Δ_T, with C_s^* an approximation to C_s.

The LES code called BOFFIN (Jones et al., 2002) was used to solve the descriptive equations. The code implements an implicit finite-volume incompressible flow solver using a co-located variable storage arrangement for all primitive variables. A linear variation between nodes is assumed, so that the value of variables at the cell faces are averages of the values at the appropriate adjacent nodes, leading to space discretisation corresponding to a central difference scheme. Fourth-order pressure smoothing based on the method of Rhie and Chow (1983) is used to prevent oscillations in the pressure field. Time advancement uses an implicit Gear method for all transport terms, with the procedure second-order accurate in space and time. A constant time step that ensured a maximum Courant number between 0.1 and 0.3 was used in the present work. This code has been used previously to predict a wide range of flows, for example, by Di Mare and Jones (2003), Bini and Jones (2008), and Yao and Fairweather (2010).

Further details of the mathematical modeling approach and numerical solution method can be found elsewhere (Bini & Jones, 2008; Di Mare & Jones, 2003).

2.2 Lagrangian particle tracking

The LPT approach was used to solve for the particle distribution in the pipe. Particles were assumed to be points, and due to the low particle concentration ($< 10^{-6}$) one-way coupling between the fluid flow and the particles was assumed, i.e. feedback to the fluid flow from the particles and particle collisions were ignored. Particle-wall

collisions were assumed to be elastic model such that all collisions resulted in a rebound back into the computational domain with no loss of kinetic energy.

The fourth-order Runge-Kutta method was used to solve the particle equations of motion for particle position and velocity according to (Zhao et al., 2020):

$$\frac{d\boldsymbol{x}_p}{dt} = \boldsymbol{V}_p \tag{12}$$

$$\frac{d\boldsymbol{V}_p}{dt} = \frac{3}{4}\frac{\rho}{\rho_p}\frac{C_D}{d_p}(\boldsymbol{V}-\boldsymbol{V}_p)\left|\boldsymbol{V}-\boldsymbol{V}_p\right| + (1-(\rho/\rho_p))\boldsymbol{g} + \boldsymbol{F}_{lift} \tag{13}$$

and $$\boldsymbol{F}_{lift} = \frac{3.08\nu^{1/2}\rho}{d_p\rho_p}\begin{pmatrix} (w-w_p)\left|\frac{\partial w}{\partial x}\right|^{1/2}\operatorname{sgn}\left|\frac{\partial w}{\partial x}\right| i + (w-w_p)\left|\frac{\partial w}{\partial y}\right|^{1/2}\operatorname{sgn}\left|\frac{\partial w}{\partial y}\right| j \\ +(v-v_p)\left|\frac{\partial v}{\partial x}\right|^{1/2}\operatorname{sgn}\left|\frac{\partial v}{\partial x}\right| i + (u-u_p)\left|\frac{\partial u}{\partial y}\right|^{1/2}\operatorname{sgn}\left|\frac{\partial u}{\partial y}\right| j \end{pmatrix} \tag{14}$$

where the subscript "p" represents variables associated with the particles. V_p, ρ_p and d_p are therefore the particle velocity, particle density and particle diameter, respectively, and V, ρ and v are the velocity, density and kinematic viscosity of the fluid, respectively. C_D is the drag coefficient given by：

$$C_D = 24(1+0.15Re_p^{0.687})/Re_p \tag{15}$$

where the particle Reynolds number $Re_p = d_p|V\text{-}V_p|/\upsilon$ (Zhao et al., 2020). The last term represents the lift force acting on particles (Winkler & Rani, 2009).

Drag, gravity, buoyancy and lift forces are all considered to affect particle motion within the turbulent pipe flow with flat bed, although other forces acting on the particles such as the Magnus force, Bassett's history force and additional mass force are all ignored since they are much smaller in comparison to the forces considered above (Armenio & Fiorotto, 2001). In addition, electrostatic forces may influence particle

behavior in pipe flows (Grosshans et al., 2021; Li et al., 2021; Yao et al., 2020), although given the focus of this work on the effect of the secondary flows the electrostatic force on particles was also excluded.

2.3 Flow configuration

As used in Liu et al. (2021b), the pipe with flat bed is defined as a circular tube with radius R, where the lower regions of the pipe are occupied by deposited particles. To simplify the problem, the floor is assumed to be flat and smooth. The height between the upper surface of the deposited bed and the top of the pipe is H, whilst the distance between the surface of the bed and the pipe center is h, where $h = 0.5R$. The spanwise length of the bed surface is L_F, and the hydraulic diameter of the pipe is D_H. A schematic diagram of the pipe geometry and coordinate system used is shown in Fig. 1(a). The flow is three dimensional and described by a Cartesian coordinate system (x, y, z) in which the z axis is aligned with the streamwise flow direction, the y axis is in the direction normal to the pipe floor, and the x axis is in the spanwise direction. The origin of the coordinate system is the center of the upper curved wall of the pipe. The pipe length in the z-direction is $L_z = 4\pi D_H$, which meets the requirements of minimum length imposed by the use of a periodic boundary condition in the streamwise direction, i.e. it is sufficiently long to accommodate the streamwise-elongated, near-wall structures present in wall-bounded shear flows (Fairweather & Yao, 2009).

The bulk Reynolds number of the flow, $Re_b = u_b D_H/\nu$, was 40,000, representative of flows found in practice, where u_b is the bulk flow velocity. Δp in the streamwise

direction was employed to keep *Re* constant. As a result, the wall shear stress, τ_w, can be calculated as follows (Nikitin & Yakhot, 2005):

$$\tau_w = \frac{\Delta p D_H}{4 L_z} \tag{16}$$

In addition, defining $u_\tau = (\tau_w/\rho)^{0.5}$, $l^* = \nu/ u_\tau$ and $t^* = l^*/ u_\tau$ then $Re_\tau = u_\tau D_H/\nu = 1{,}700$. For the particles, $\rho_p/\rho = 1224$, $d_p = 5$ and 50 μm, the particle relaxation time $\tau_p = \rho_p d_p^2/18\rho\nu$, and with $St = \tau_p u_\tau^2/\nu$, the Stokes numbers of the particles are 0.6 and 63, respectively. The Shields number θ (defined as $\theta = \tau_w/(\rho_p-\rho)g d_p$) for the particles is 1.4 and 0.1 for the 5 and 50 μm particles, respectively. The number of 5 and 50 μm particles considered in the pipe was 5×10^5 and 5×10^4, respectively, where the average volume fraction of the particles is significantly less that 10^{-6}.

The numerical grid used in the predictions of the pipe with flat bed is shown in cross-section in Fig. 1(b), with only part of the full grid, which consisted of 250 × 76 nodes over the cross-section, shown for the sake of clarity. Part of the mesh at the center of the pipe is folded (highlighted in the inset of the figure), and the upper mesh line has two overlapping nodes. Such grid generation depends on solution of the Poisson equation (Liu et al., 2021b), which may diverge if overlapping nodes are used as a boundary condition. To obtain an effective solution, the layer above ($\eta = 2$) has its grid shape designed as rectangle. Once the information on grids with $\eta > 2$ is obtained that about the $\eta = 2$ layer can be determined by using neighboring grids. The triangular mesh in the very center is also much smaller than elsewhere, and flow information is obtained by interpolating variable values at grid points on the line $\eta = 2$ from the previous time step.

A no-slip boundary condition was imposed at the solid surfaces and a periodic boundary condition was imposed at the inlet and outlet. The complete mesh consisted of 250 × 76 × 100 nodes (i.e. 1.9M nodes in total), spaced equally in the streamwise direction, and expanded exponentially away from the wall with the first node located at $y^+ = 0.5$. The time step was automatically adjusted to ensure that the Courant number was always less than 0.5.

2.4 Validation

To validate predictions of the overall model described, the flow field in pipes with $H = 0.7R$ and $H = 2R$ (i.e. a full circular pipe) with a similar Reynolds number to that used in the present work were simulated as noted above. As shown in Fig. 2(a1) and 2(a2), the simulated mean spanwise velocity is in reasonable agreement with the experimental data of Larsson et al. (2011). In addition, in Fig. (a3) and a(4), the mean and fluctuating velocities simulated in the full pipe with H=2R agree well with the results of DNS simulations (Wu & Moin, 2008), with the predicted normal stresses in the Larsson et al. (2011) flow, Fig. 2(b1)-(b2), also in acceptable agreement with their data. In this work, the pipe flow with a flat bed has $H = 1.5R$ and two grids were used to investigate the impact of grid resolution on the predictions, Fig. 2(c1)-(c4). A relatively sparse grid, with 180 × 60 nodes in the pipe cross-section, and a finer grid with 250 × 76 nodes in the cross-section were employed, with both having 100 nodes distributed in the streamwise direction. As shown in Fig. 2(b1)-(b4), the results obtained

using both grids are reasonably close, indicating adequate resolution using the more refined mesh.

3. Results and discussion

3.1 Flow field

The instantaneous flow field in the pipe with flat bed is shown in Fig. 3, where the turbulence structure at grid scale has been resolved. It is known (Huser & Biringen, 1993) that the interaction between burst events near the two adjacent walls in the corner of the pipe cause the secondary flow. Instantaneous streamwise vorticity contours in Fig. 3(a) show the complexity of the turbulent flow and differences at various flow scales. A top view of the instantaneous streamwise velocity in the $(y+h)^+ = 10$ plane is shown in Fig. 3(b). Due to side wall effects, the number of low and high speed streaks near the pipe corners is less than near the center of the floor which agrees with the findings of (Noorani et al., 2016).

Instantaneous cross-stream streamlines in the cross-section of the pipe flow with flat bed are shown in Fig. 4(a). It is clear that the streamwise vortices near the pipe floor are denser than those towards the top of the pipe, most likely due to the effect of the pipe corners. This in turn may lead particles to be more dispersed in particle-laden flows. Secondary flows can be found in the flow. Average streamlines are shown in Fig. 4(b), where two large vortices exist in the upper regions of the pipe, with two smaller vortices below. Such vortices look different to those observed in a square duct flow (as illustrated in Fig. 4(c) from Wang et al. (2019)), where symmetry causes the vortices to

be of the same size. As noted, the mechanism by which the secondary flow is formed is due to turbulence interaction near the corners of the pipe wall (Huser & Biringen, 1993; Yao & Fairweather, 2010), with the large vortices generated due to the upper wall being longer than the floor in the pipe cross-section which is caused by the flat bed (Liu et al., 2021a; Vinuesa et al., 2014; Vinuesa et al., 2016). This is similar to the mechanism which forms secondary flows in a rectangular duct (as illustrated in Fig. 4(d)). In addition, such secondary flows can also be found in elliptic pipes (Nikitin & Yakhot, 2005) as well as in square ducts with round corners (Vidal et al., 2017) due to the curvature variation of the wall (Eggels et al., 2006).

The time-averaged magnitude of the secondary flow velocity and intensity is shown in the left half of Fig. 5(a). The vectors indicate the secondary flow direction as well as the flow pattern, which demonstrates that the secondary flow intensity is higher near the wall and the corner bisectors, as in square ducts flows (Vinuesa et al., 2014). In the pipe with bed, secondary vortices near the side wall are modified, occupying the whole space from the wall to the center-plane, as found in large aspect ratio rectangular ducts (Vinuesa et al., 2014). In addition, Fig. 5(a) also shows that contours of the average streamwise velocity bulge towards the corners, also as in square duct flows (Pirozzoli et al., 2018). Figure 5(b) shows the turbulence kinetic energy in the pipe cross-section, where it is found to be high near the wall in agreement with the findings in other pipe flows (El Khoury et al., 2013). However, at the top of the pipe it is found to be lower, most likely caused by the interaction between the upper two vortices. The turbulence kinetic energy is also low in the corner bisector region due to the transport

effect of the secondary flow. In addition, and similar to flows in square and rectangular ducts (Noorani et al., 2016), a zero-energy region is found in close proximity to the corners due to the inhibiting effect of the side walls.

The four velocity profiles shown in Fig. 6 (at y/R = -0.2, 0.1, 0.4, 0.7) present the flow motion quantitatively. For the spanwise velocity (Fig. 6(a)) along the lines y/R = -0.2 and 0.1, as $x > 0$, $\overline{u}^+$ is greater than 0 (except near the wall) and its maximum $\overline{u}^+_{\max}$ = 0.2. Along the line y/R = 0.4, the spanwise velocity near the center (-0.5 < x/R < 0.5) is fairly low, where the flow moves away from the center towards the corners. The spanwise velocity trend at y/R = 0.7 is also approximately the opposite of that at y/R = -0.2. For the four profiles shown in Fig. 6(a), the maximum spanwise velocity for each case is similar in magnitude. In the vertical direction shown in Fig. 6(b), for each profile, the flow velocity reaches its positive maximum near the side walls. At y/R = 0.1, near the side wall, the flow vertical velocity $\overline{v}^+$ is at a maximum in the flow (0.4), whilst at y/R = -0.2, the vertical velocity $\overline{v}^+$ at the midpoint is positive while negative values occur for all other profiles. Figure 6 is therefore useful in characterising the average secondary flow velocity in the pipe flow with flat bed which is subsequently helpful in understanding particle behavior.

Figure 7 shows the flow mean velocity in the pipe cross-section averaged in time and along the streamwise direction near the floor (Fig. 7(a) and (b)) and upper wall (Fig. 7(c) and (d)). In the pipe, the secondary flow originates from the interactions of turbulence in the corners. As a result, the magnitude of the flow velocity in the cross-section is related to burst events and their interactions, especially near the wall. Figure

7 (a) shows that near the floor, at $(y+h)^+ = 10, 50, 100$, the spanwise velocity $\overline{u}^+$ reaches a negative maximum at $x/D_H = 0.45$, 0.35 and 0.25, respectively. The spanwise velocity therefore reaches a maximum away from the pipe floor and the corners. A similar phenomenon can be found in square duct flows (Pirozzoli et al., 2018). In addition, the maxima in $\overline{u}^+$ at $(y+h)^+ = 10$ and 50 are very similar, whilst that at $(y+h)^+ = 100$ is obviously smaller. This can be explained by the fact that the area between $(y+h)^+ = 10$ and 50 is the dominant region for burst events, while in the farther region ($(y+h)^+ > 50$), burst events near the wall no longer have a direct effect on the flow. Since the side wall is not perpendicular to the floor, the further away from the floor, the less variation in $\overline{u}^+$ in the spanwise direction, with $\overline{u}^+$ being positive near the corner ($x/D_H > 0.51$) at $(y+h)^+ = 10, 50, 100$ corresponding to the velocity of the upper vortices above the corner bisector.

At $(y+h)^+ = 10$, the average flow velocity $\overline{v}^+ < 0.5$ is only $1/10^{th}$ of $\overline{u}^+$ at the same $(y+h)^+$ value. The vertical velocity v near the floor can be derived from flow continuity and, due to wall effects, the velocity in the vertical direction is fairly low. At $(y+h)^+ = 50, 100$, the maximum $\overline{v}^+$ approaches 3 but is still less than the velocity in the spanwise direction. In addition, at $x/D_H < 0.3$, the average flow velocity in the vertical direction at $(y+h)^+ = 50, 100$ is mostly greater than zero indicating that the flow is moving from the wall to the center of the pipe under the effect of the secondary flow, which is far away from the corner and with a magnitude less than 1. Similar to Fig.7(a), a positive vertical velocity can be found near the corner corresponding to the upward secondary flow near the side wall.

The profile of the average circumferential velocity $\overline{u}_t^+$ near the upper wall is similar to that of the spanwise velocity near the floor (as shown in Fig. 7(c)). However, compared with the latter, the circumferential velocity at $(y+h)^+ = 10$ near the upper wall is smaller, whilst that at $(y+h)^+=100$ is larger, than the equivalent spanwise velocity, indicating that the flow velocity associated with the upper vortices is high. In addition, the magnitude of the radial velocity near the upper wall is similar to that of the vertical velocity near the floor (as shown in Fig. 7(d)). It is known (Liu et al., 2021b) that the upper wall is 2.42 times longer than the length of the floor and that the upper vortices tend to circulate throughout the whole higher regions of the pipe (Fig. 5) which is quite different from that occurring in a rectangular duct with large aspect ratio (Noorani, et al., 2016).

Average streamwise vorticity contours (Fig. 8) show that the vorticity centers associated with the lower and upper vortices are (± 0.51, -0.25) and (± 0.46, -0.27), normalized by D_H, respectively. That is, their distances from the corner are 0.044 and 0.056, and distances from the adjacent wall are 0.020 and 0.024, respectively. It is noted that the distance from the streamline centers of the upper vortices to the corner is 2.68 times that from the centers of the lower vortices to the corner, and the ration of the distance to the adjacent wall is 2.62. Therefore, although the streamline centers of the lower vortices are much closer to the corner and the wall under the wall restriction (Liu et al., 2021a, 2021b), the vorticity center does not have this property. This is because the vorticity field depends on the near-wall turbulence structure, and the length of the adjacent wall has no significant effect on vorticity (Vinuesa et al., 2014, 2016). Similar

phenomenon can also be found in a rectangular duct flow with large aspect ratio (as shown in Fig. 8(c)), although the secondary streamline pattern extends more close to the long side of the duct than near the shorter side, although the development of vorticity along both sides of the duct is similar (Vinuesa et al., 2014, 2016). It should be noted that the extension of the high vorticity areas near the wall is opposite in direction to that of the secondary vortices, which is related to the wall length and similar to the secondary flows in rectangular ducts. This is likely due to the fact that vorticity in the same direction as the secondary flow originates from the velocity gradient perpendicular to the wall, while the vorticity near the wall originates from the velocity gradient parallel to the wall. Geometrically, a pipe flow with flat bed is quite different from that in a rectangular duct. As a result, the secondary flows formed in them are different, as is the streamwise vorticity.

In addition, the vorticity near the floor (± 0.2 - ± 1) is slightly larger, but not significantly different from, that near the upper wall (± 0.2 - ± 0.8). It is found that the magnitude of vorticity in a pipe flow with flat bed is therefore equivalent to that in other non-circular duct flows, such as in a turbulent hexagonal duct (Marin et al., 2016).

Isosurfaces of the instantaneous streamwise velocity are show in Fig. 9 for w = 1.15u_b and 1.2u_b. Large turbulent structures are observed in the streamwise direction, although they are not continuous, in contrast to flow in a hexagonal duct with Re_b = 11,700 where continuous isosurfaces of velocity for w = 1.2u_b are found (Marin et al., 2016). It can be seen that in this work, with Re_b = 40,000, the equivalent surface is disjointed within the pipe. It may therefore be concluded that small turbulent structures

occurring at high Reynolds number do not reflect the macroscopic geometric constraints imposed in such pipe flows.

3.2 Particle distribution

To describe particle deposition quantitively, the particle deposition rate R_d is introduced as follows:

$$R_d = \frac{n_d(t_2) - n_d(t_1)}{(t_2 - t_1) \cdot n_t} \tag{17}$$

where $n_d(t_1)$ and $n_d(t_2)$ are the number of particles deposited on the pipe floor at time t_1 and t_2, respectively, and n_t is the total number of particles considered in the pipe. From $t^+ = 0$ to 3,700, the deposition rate of 5μm particle ($St = 0.6$) was equal to zero (as shown in Fig. 10), suggesting, as might be anticipated for such low Stokes number particles, very little or no deposition within the flow. For the 50μm ($St = 63$) particles, the deposition trend is significantly different from that of the smaller particles and can be divided into several intervals. First, in the period $t^+ = 0$-500, the deposition rate of 50μm particles is approximately zero, similar to that of the 5μm particles. This is due to the inertia effect. It therefore takes a significant time for large particles to follow the local fluid and move forward within the flow and then start to deposit. After, from $t^+ =$ 500-1000, the slip velocity between the particles and the local fluid flow consumes particle energy that leads to particle deposition under the effect of gravity. Furthermore, from $t^+ = 1500$-3000, the particle deposition rate becomes approximately constant. By $t^+ = 3000$, most of the particles have deposited on the floor of the pipe (70%), after which the deposition rate decreases until all are deposited on the floor. From $t^+ =$0~3700,

the maximum volume fraction of the 50μm particles is less than 10^{-6} so the assumption of one-way coupling used in this work is justified (Elghobashi, 1994).

Fig. 11 shows the instantaneous distribution of 50 μm particles at $t^+ = 800$. At this time, the particles have started to deposit on the floor of the pipe with particle-free regions in the upper part of the pipe. Those deposited near the pipe floor are preferentially concentrated in streamwise orientated low speed streaks that are characteristic of the viscous sublayer and caused by the burst-sweep cycle. It is worth noting that these streaks are more obvious towards the center of the flow due to the impact of the secondary flows in the lower regions of the pipe. Similar to the particle distributions found in square and rectangular ducts (Fairweather & Yao, 2009; Noorani et al., 2016), preferential concentration of particles can also be found in the pipe corners which is due to the secondary flow moving from the pipe center to the corners. In addition, and because of the inward curve of the wall towards the pipe floor, particles near the curved wall tend to deposit towards the corners under the effect of gravity effect, as can be seen in Fig. 11(a).

Figure 12 shows the instantaneous distribution of 5μm and 50μm particles. It is known that turbulent secondary flows affect particle behavior in square duct flows (Yao & Fairweather, 2010). Generally, in the pipe, the 5μm particles do not move with the secondary flow with their behavior dictated by coherent turbulent structures. The larger 50μm particles tend to deposit on the floor as noted above and as studied in previous work (Liu et al., 2021a, 2021b). A stable structure of particle distribution in the cross-section cannot be found due to the effects of gravity, with the motion of most particles

directed downwards and unlikely to move upwards under the influence of the secondary flow (Liu et al., 2021a). Near the pipe center and side walls, under the influence of the secondary flows, the particles tend to fall slower in comparison with those in other regions. Therefore, the 50μm particles tend to concentrate near the pipe center and side walls in the pipe with flat bed. In addition, the large particle distribution along the wall above the corner depends on particles sliding along the inclined wall under the effect of gravity.

Figure 13 shows the average particle velocity and slip velocity at y/R=-0.2, 0.1, 0.4, 0.7. Figure 13(a) gives the average spanwise velocity of particles indicating that in this direction, the particles follow the flow independent of particle size, with their velocities in the spanwise direction being very similar. Figure 13(b) shows that the average vertical velocities of the 5μm particles are almost the same as those of the fluid, with the vertical slip velocity close to zero (Fig. 13(d)). The average vertical velocities of the 50μm particles are negatively deviated from those of the smaller particles. The maximum (negative) particle velocity occurs at the midpoint of the lines y/R = 0.1, 0.4, 0.7, reaching -0.5, where the local fluid velocity is directed exactly downwards. Figure 13(c) shows the average slip velocity for the particles, where this velocity refers to the velocity difference between particles and the local fluid flow (u_g and v_g). It can be seen that the average slip velocity of the 50μm particles is significantly different from that of the 5μm particles, with the maximum spanwise slip velocity of the 50μm particles being 0.1 whilst that of the 5μm particles is essentially zero. These differences are also reflected in the predictions shown in Fig. 13(a), with the difference in the velocity of

the particles decreasing with y/R due to the particle velocity decreasing as the flow approaches the floor of the pipe. Figure 13(d) shows the vertical slip velocity for the particles. Here, it can be seen that the profiles are consistent with the average vertical velocities of the particles shown in Fig. 13(b), with the vertical slip velocity of the 5μm particles approximately zero, whilst those of the 50μm particles are approximately constant (-0.2~-0.3) in the x-direction.

Average velocity contours of the particles are shown in the left half of Fig. 14(a) and (b), with streamwise velocity contours shown in right half of these plots. The difference in velocity between the particles and the local fluid flow is shown in Fig. 15. The vectors in Figs. 14 and 15 represent the time-averaged motion of the particles, where they are scaled by the bulk velocity u_b. It can be seen that the velocity of the 5μm particle is very similar to that of the local fluid flow whilst that of the 50μm particles is significantly different. This is in contrast to the findings of Noorani et al. (2016) who found no significant change in particle velocity with varying sizes of particle, essentially because the effects of gravity were not accounted for. It is known that the drag force is 0-50 times greater than that of gravity for the 5μm particles and 0-5 times greater for the 50μm particles (Liu et al., 2021b). The schematic diagram shown in Fig. 16 illustrates the secondary motion in this pipe. Due to the secondary flow effect caused by the flat bed, the particles tend to deposit with the average downward flow velocity close to the corner in the corner bisector region, and at the junction region between the two vortices. Combined with the effect of gravity, the velocity of the 50μm particles reaches a maximum in both regions, as shown in Fig. 14(b). In contrast, near the side

walls, the secondary flow tends to promote the movement of particles upwards against gravity, with the velocity of the 50μm particles reaching its minimum value on this region, as shown in Fig. 14(b). The flow velocity is small in the light grey area in Fig. 16, as indicated in Fig. 5(a), so particle motion in this region is mostly influenced by inertia and gravity. Therefore, the velocities of the 50μm particles near the pipe floor are found to be large, as shown in Fig. 14(b). In addition, for the velocity in the streamwise direction, the difference between the two sizes of particles and the local flow velocity (Figs. 14 and 15) is not obvious, which is similar to that found in square and rectangular duct flows (Noorani et al., 2016).

As noted above, the slip velocity of the 5μm particles is considerably different from that of the 50μm particles. For the 5μm particles, their velocity is lower than that of the local flow near the pipe floor and side walls, while this trend is reversed in other areas of the flow. In the work of Noorani et al. (2016), the particle velocity is found to be higher than that of the local flow near the corner bisector, and particularly near the upper part of the side walls in both square and rectangular ducts, when gravity is ignored. Due to the effect of gravity, however, the 5μm particle concentration decreases significantly in the upper regions of the pipe (Liu et al., 2021b). Under the effects of particle inertia, as a particle moves from a region of high secondary flow intensity to others at a lower level, the slip velocity becomes so large that the velocities of the particles near the upper side wall, as well as near the corner bisector, become faster than the local flow velocity. For the 50μm particles, their velocities are lower than the local flow velocity near the side wall, floor and corner, but significantly higher than the local

flow velocity in other regions of the flow. Since gravity and drag are of the same order of magnitude (Liu et al., 2021b), their synergistic effect on the particles is complex, as illustrated in Fig. 16. Near the side wall, the upward velocity of the particles is decreased by the effect of gravity. Similarly, near the floor the particle velocity decreases due to the effect of the wall and the slip velocity becomes negative. In other regions of the flow, the downward velocity of the particles is increased by the gravity effect and the slip velocity becomes positive.

Fig. 17 shows contours of the turbulence kinetic energy of the particles in the cross-section of the pipe. For the particles, the kinetic energy is defined as $\overline{u'_{ip}u'_{ip}}/2$, where the superscript represents the fluctuation of the particle velocity about the mean. It is seen that kinetic energy of the 5μm particles is higher than that of the 50μm particles near the pipe center and the floor, which has also been found to be the case in channel (Picciotto et al., 2005), pipe (Portela et al., 2002) and duct (Noorani et al., 2016) flows because the inertia of the large particles works against the flow turbulence. However, at the top of the pipe, the kinetic energy of the 50μm particles is higher than that of the 5μm.

Figure 18 shows the particle deposition rate on the pipe floor and the resuspension from it, with similar results given in Fig. 19 relative to the curved wall of the pipe. The resuspension (V_{res}) and deposition (V_{dep}) rate of the particles can be respectively calculated by the ratio of the flux J_{res} and J_{dep} of particles passing through $(y+h)^+=10$, 50, 100 or $(R-\sqrt{x^2+y^2})^+=10$, 50, 100 to the particle concentration C in the whole pipe, as given in Eqs. (18) and (19):

$$V_{res} = J_{res} / C \tag{18}$$

$$V_{dep} = J_{dep} / C \tag{19}$$

Particles moving from the wall to the center of the flow are considered in the particle resuspension flux J_{res}. In contrast, particles moving from center to the wall are considered in the particle deposition flux J_{dep}.

Figure 18(a) shows that the 5μm particle deposition rate is high near the floor center and corner. In a square duct flow, Yao and Fairweather (2012) found that small particles (St < 6.43) tend to deposit in the floor center but large particles (St > 12.38) deposit in the corner. In this work, differences in the deposition of 5μm particles (St = 0.6) are caused by the downward sliding of particles along the sloped side wall in this pipe. Figure 18(b) shows that the deposition rate of 50μm particles (St = 63) reaches its highest level at the corner, similar to that found in a square duct (Yao & Fairweather, 2012).

In terms of the resuspension rate, Yao and Fairweather (2010) found that particles in a square duct tend to move upwards near the floor center and the corner, which is also true in the present pipe flow with flat bed. The difference between the two geometries is that, for the 5μm particles, the deposition rate reaches its highest level in this work at x/D_H = 0.3 due to the high intensity of the secondary flow locally (as shown in Fig. 7(a)). In addition, the Reynolds number considered by Yao and Fairweather (2010) was significantly higher than that of the present work, at Re = 250k.

Near the pipe floor, it is worthy of note that for the 5μm particles a lower rate of particle deposition and resuspension occurs on moving closer to the floor, whilst for the

50μm particles the highest deposition and resuspension rates are found at $(y+h)^+=10$. The 5μm particles are slightly further away from the wall, at $(y+h)^+=100$, when their deposition and resuspension rates are high, and they are easily trapped in the viscous sublayer (Noorani et al., 2016) as well as resuspended at the pipe center under the effect of the secondary flow. However, for the 50μm particles gravity effects dominate their behavior as they deposit on the pipe floor.

The deposition and resuspension rates of particles near the curved wall of the pipe are given in Fig. 19. Unlike deposition near the pipe floor, the deposition rate of 5μm particles near this wall shows an increasing trend from the wall center to the corner (at $\theta=\pm 2/3\pi$ shown in Fig. 7) which is more obvious than is found for the 50μm particles. This can be explained by the effect of the secondary flow moving towards the corner, as well as gravity increasing deposition in the downward direction. The maximum resuspension rate of the 5μm particles occurs near $\theta=1/2\pi$ at $(R-\sqrt{x^2+y^2})^+=50, 100$. Particles leave the upper wall of the pipe at $\theta=0$ under the influence of the secondary flow and gravity, but are unable to return to top of the pipe resulting in a low resuspension rate at the upper wall. Similar to particle resuspension near the floor, the 50μm particles near the upper wall have a high resuspension rate near the corner. Compared with the planes further from the wall, the resuspension rate of particles passing through $(R-\sqrt{x^2+y^2})^+=10$ is less than that in the region $\theta<1/2\pi$ and greater than that in $\theta>1/2\pi$. Because the radial flow velocity $\overline{v}^+$ at $(R-\sqrt{x^2+y^2})^+=10$ is fairly low, particle behavior is dominated by gravity and few particles are found in the region $\theta<1/2\pi$ with more found at $\theta<1/2\pi$. Finally, the closer the 5μm particles approach

the upper wall, the lower the deposition and resuspension rates, which is similar to that found near the pipe floor.

4. Conclusions

Under the assumption of particles being deposited on a pipe floor forming a smooth and horizontal bed, large eddy simulation, one-way coupled with a Lagrangian particle tracking method, has been used to characterise the flow field and distribution of $5\mu m$ and $50\mu m$ diameter particles in a $Re_b = 40{,}000$ flow with bed height $h = 0.5R$.

Turbulent secondary flows were found in the pipe flow with a flat bed, and the corner in the pipe cross-section caused by the flat bed is the source of the secondary flows. These flows are generated because of the interaction of burst events, including ejection and sweep events near the pipe corners. The upper pipe wall affects the secondary flow formation as its curvature restricts ejection but promotes sweep events. Due to this restriction, a large pair of upper vortices are formed, above two smaller vortices close to the pipe floor, which extend further towards the pipe center than the lower vortices.

The overall deposition rate of $5\mu m$ particles was found to be close to zero. However, under the action of gravity and the secondary flows, the $50\mu m$ particles deposited forming irregular elongated particle streaks associated with low speed streaks close to the pipe floor, these being more prominent towards the center of the flow due to the impact of the secondary flows in the lower regions of the pipe. Preferential concentration of these particles was also found in the pipe corners due to the secondary

flow moving towards the corners from the pipe center. Both types of particle were found to have similar average spanwise velocities while their vertical velocities were significantly different due to the effects of gravity. The average vertical velocity of the 5μm particles was therefore close to that of the local secondary flow whilst for the 50μm particles the corresponding velocity was large, and negatively deviated from that of the smaller particles, at the conjunction area of the upper vortices and near the floor, again caused by the combined effects of the secondary flow and gravity.

The deposition rate of the 5μm particles was high near the center of the floor and at the pipe corners, while that of the 50μm particles was greatest near the corners, similar to as is found in particle-laden square duct flows. The resuspension of particles was greatest near the floor center and the pipe corners, again as found in duct flows. Lastly, deposition and resuspension rates of particles near the curved wall of the pipe showed an increasing deposition rate for the 5μm particles moving from the wall center to the corners, which was greater than was found for the larger particles, due to the effects of the secondary flow moving towards the corner. The maximum resuspension rate of the 5μm particles occurred above the pipe corners with a lower resuspension rate on the upper wall under the influence of the secondary flow and gravity, with the 50μm particles showing their highest resuspension rate above and at the corner of the pipe.

Acknowledgements

This work was supported by the National Natural Science Foundation of China (No. 51876225; 51776221) and the High-end Foreign Expert Introduction Project

(G20190001270; B18054). The authors also gratefully acknowledged the financial support from the China Scholarship Council.

Data availability

The data that support the findings of this study are available from the corresponding author upon reasonable request.

References

Adams, J. F. W., Fairweather, M., & Yao, J. (2011). Particle deposition in circular pipes with variable bed height. In *13th European Turbulence Conference (ETC13)* (Vol. 318, pp. 052001).

Almeida, T. G., & Jaberi, F. A. (2008). Large-eddy simulation of a dispersed particle-laden turbulent round jet. *International Journal of Heat and Mass Transfer, 51*, 683-695.

Armenio, V., & Fiorotto, V. (2001). The importance of the forces acting on particles in turbulent flows. *Physics of Fluids, 13*, 2437-2440.

Arolla, S. K., & Desjardins, O. (2015). Transport modeling of sedimenting particles in a turbulent pipe flow using Euler–Lagrange large eddy simulation. *International Journal of Multiphase Flow, 75*, 1-11.

Battista, F., Mollicone, J. P., Gualtieri, P., Messina, R., & Casciola, C. M. (2019). Exact regularized point particle (ERPP) method for particle-laden wall-bounded flows in the two-way coupling regime. *Journal of Fluid Mechanics, 878*, 420-444.

Bini, M., & Jones, W. P. (2008). Large-eddy simulation of particle-laden turbulent flows. *Journal of Fluid Mechanics, 614*, 207-252.

Bradshaw, P. (1987). Turbulent Secondary Flows. *Annual Review of Fluid Mechanics, 19*, 53-74.

Brundrett, E., & Baines, W. (1964). The Production and Diffusion of Vorticity in Duct Flow. *Journal of Fluid Mechanics, 19*, 375-394.

Cantwell, B. J. (2019). A universal velocity profile for smooth wall pipe flow. *Journal of Fluid Mechanics, 878*, 834-874.

Di Mare, L., & Jones, W. (2003). LES of turbulent flow past a swept fence. *International Journal of Heat and Fluid Flow, 24*, 606-615.

Dritselis, C. D., & Vlachos, N. S. (2011). Large eddy simulation of gas-particle turbulent channel flow with momentum exchange between the phases. *International Journal of Multiphase Flow, 37*, 706-721.

Eggels, J. G. M., Unger, F., Weiss, M. H., Westerweel, J., Adrian, R. J., Friedrich, R., & Nieuwstadt, F. T. M. (2006). Fully developed turbulent pipe flow: a comparison between direct numerical simulation and experiment. *Journal of Fluid Mechanics, 268*, 175-210.

El Hasadi, Y., Busedra, A. A., & Rustum, I. M. (2007). Laminar Mixed Convection in the Entrance Region of Horizontal Semicircular Ducts With the Flat Wall at the Top. *Journal of Heat Transfer, 129*, 1203-1211.

El Khoury, G. K., Schlatter, P., Noorani, A., Fischer, P. F., Brethouwer, G., & Johansson, A. V. (2013). Direct Numerical Simulation of Turbulent Pipe Flow at Moderately High Reynolds Numbers. *Flow, Turbulence and Combustion, 91*, 475-495.

Elghobashi, S. (1994). On predicting particle-laden turbulent flows. *Applied scientific research, 52*, 309-329.

Fairweather, M., & Yao, J. (2009). Mechanisms of particle dispersion in a turbulent, square duct flow. *AIChE Journal, 55*, 1667-1679.

Fröhlich, K., Schneiders, L., Meinke, M., & Schröder, W. (2018). Validation of Lagrangian Two-Way Coupled Point-Particle Models in Large-Eddy Simulations. *Flow, Turbulence and Combustion, 101*, 317-341.

Gallen, L., Felden, A., Riber, E., & Cuenot, B. (2019). Lagrangian tracking of soot particles in LES of gas turbines. *Proceedings of the Combustion Institute, 37*, 5429-5436.

Gavrilakis, S. (1992). Numerical simulation of low-Reynolds-number turbulent flow through a straight square duct. *Journal of Fluid Mechanics, 244*, 101-129.

Grosshans, H., Bissinger, C., Calero, M., & Papalexandris, M. V. (2021). The effect of electrostatic charges on particle-laden duct flows. *Journal of Fluid Mechanics, 909, A21*.

Hurst, K., & Rapley, C. (1991). Turbulent flow measurements in a 30/60 degree right triangular duct. *International Journal of Heat and Mass Transfer, 34*, 739-748.

Huser, A., & Biringen, S. (1993). Direct numerical simulation of turbulent flow in a square duct. *Journal of Fluid Mechanics, 257*, 65-95.

Jones, W. P., di Mare, F., & Marquis, A. J. (2002). *LES-BOFFIN : User's guide*. London: Technical Memorandum, Department of Mechanical Engineering, Imperial College of Science, Technology and Medicine.

Kasper, R., Turnow, J., & Kornev, N. (2019). Multiphase Eulerian–Lagrangian LES of particulate fouling on structured heat transfer surfaces. *International Journal of Heat and Fluid Flow, 79*, 108462.

Kriebitzsch, S., & Richter, A. (2020). LES simulation of char particle gasification at Reynolds numbers up to 1000. *Combustion and Flame, 211*, 185-194.

Larsson, I., Lindmark, E., Lundström, T., & Nathan, G. (2011). Secondary Flow in Semi-Circular Ducts. *Journal of Fluids Engineering, 133*, 101206-101214.

Li, J., Yao, J., Zhao, Y., & Wang, C.-H. (2021). Large eddy simulation of electrostatic effect on particle transport in particle-laden turbulent pipe flows. *Journal of Electrostatics, 109*, 103542.

Lin, Z., Shao, X., Yu, Z., & Wang, L. (2017). Effects of finite-size heavy particles on the turbulent flows in a square duct. *Journal of Hydrodynamics, 29*, 272-282.

Lin, Z., Yu, Z., Shao, X., & Wang, L. (2017). Effects of finite-size neutrally buoyant particles on the turbulent flows in a square duct. *Physics of Fluids, 29*, 103304.

Liu, M., Yao, J., & Zhao, Y. (2021a). The dispersion of particles in turbulent semi-circular duct flows. *Petroleum Science, 18*, 1240-1255.

Liu, M., Yao, J., & Zhao, Y. (2021b). Particle dispersion in turbulent sedimentary duct flows. *Advanced Powder Technology, 32*, 4245-4262.

Luo, K., Fan, J., Jin, H., & Cen, K. (2004). LES of the turbulent coherent structures and particle dispersion in the gas–solid wake flows. *Powder Technology, 147*, 49-58.

Madabhushi, R., & Vanka, S. (1991). Large eddy simulation of turbulence‐driven secondary flow in a square duct. *Physics of Fluids, 3*, 2734-2745.

Marin, O., Vinuesa, R., Obabko, A., & Schlatter, P. (2016). Characterization of the secondary flow in hexagonal ducts. *Physics of Fluids, 28*, 125101.

Moinuddin, K. A. M., Joubert, P. N., & Chong, M. S. (2004). Experimental investigation of turbulence-driven secondary motion over a streamwise external corner. *Journal of Fluid Mechanics, 511*, 1-23.

Nagata, K., Hunt, J. C. R., Sakai, Y., & Wong, H. (2010). Distorted turbulence and secondary flow near right-angled plates. *Journal of Fluid Mechanics, 668*, 446-479.

Nikitin, N., & Yakhot, A. (2005). Direct numerical simulation of turbulent flow in elliptical ducts. *Journal of Fluid Mechanics, 532*, 141-164.

Nikuradse, J. (1930). Turbulent Strömung in nicht kreisförmigen Rohren. *Ingenieur-Archiv, 1*, 306-332.

Noorani, A., Vinuesa, R., Brandt, L., & Schlatter, P. (2016). Aspect ratio effect on particle transport in turbulent duct flows. *Physics of Fluids, 28*, 115103.

Pakseresht, P., & Apte, S. V. (2019). Volumetric displacement effects in Euler-Lagrange LES of particle-laden jet flows. *International Journal of Multiphase Flow, 113*, 16-32.

Peng, C., Geneva, N., Guo, Z., & Wang, L.-P. (2018). Direct numerical simulation of turbulent pipe flow using the lattice Boltzmann method. *Journal of Computational Physics, 357*, 16-42.

Picciotto, M., Marchioli, C., & Soldati, A. (2005). Characterization of near-wall accumulation regions for inertial particles in turbulent boundary layers. *Physics of Fluids, 17*, 098101.

Piomelli, U., & Liu, J. (1995). Large‐eddy simulation of rotating channel flows using a localized dynamic model. *Physics of Fluids, 7*, 839-848.

Pirozzoli, S., Modesti, D., Orlandi, P., & Grasso, F. (2018). Turbulence and secondary motions in square duct flow. *Journal of Fluid Mechanics, 840*, 631-655.

Portela, L. M., Cota, P., & Oliemans, R. V. A. (2002). Numerical study of the near-wall behaviour of particles in turbulent pipe flows. *Powder Technology, 125*, 149-157.

Prandtl, L. (1926). Über die ausgebildete turbulenz. In *2nd International Congress for Applied Mechanics*. Zurich, 12-17 September 1926.

Rabencov, B., & van Hout, R. (2015). Voronoi analysis of beads suspended in a turbulent square channel flow. *International Journal of Multiphase Flow, 68*, 10-13.

Rhie, C., & Chow, W. (1983). Numerical study of the turbulent flow past an airfoil with trailing edge separation. *AIAA Journal, 21*, 1525-1532.

Rice, H. P., Fairweather, M., Hunter, T. N., Peakall, J., & Biggs, S. R. (2017). The influence of relative fluid depth on initial bedform dynamics in closed, horizontal pipe flow. *International Journal of Multiphase Flow, 93*, 1-16.

Sharma, G., & Phares, D. J. (2006). Turbulent transport of particles in a straight square duct. *International Journal of Multiphase Flow, 32*, 823-837.

Sherik, A. M., Zaidi, S. R., & Tuzan, E. V. (2008). *Black powder in gas transmission systems*. CORROSION 2008, New Orleans, Louisiana: NACE-08415.

Smagorinsky, J. (1963). General Circulation Experiments with the Primitive Equations. *Monthly Weather Review, 91*, 99-164.

Vidal, A., Vinuesa, R., Schlatter, P., & Nagib, H. (2017). Influence of corner geometry on the secondary flow in turbulent square ducts. *International Journal of Heat and Fluid Flow, 67*, 69-78.

Vinuesa, R., Noorani, A., Lozano-Durán, A., Khoury, G., Schlatter, P., Fischer, P., & Nagib, H. (2014). Aspect ratio effects in turbulent duct flows studied through direct numerical simulation. *Journal of Turbulence, 15*, 677-706.

Vinuesa, R., Prus, C., Schlatter, P., & Nagib, H. (2016). Convergence of numerical simulations of turbulent wall-bounded flows and mean cross-flow structure of rectangular ducts. *Meccanica, 51*, 3025-3042.

Wang, Q., & Squires, K. (1996). Large Eddy Simulation of Particle Deposition in a Vertical Turbulent Channel Flow. *International Journal of Multiphase Flow, 22*, 667-683.

Wang, Y., Zhao, Y., & Yao, J. (2019). Large eddy simulation of particle deposition and resuspension in turbulent duct flows. *Advanced Powder Technology, 30*, 656-671.

Winkler, C. M., & Rani, S. L. (2009). Relative importance of the lift force on heavy particles due to turbulence driven secondary flows. *Powder Technology, 190*, 310-318.

Wu, X., & Moin, P. (2008). A direct numerical simulation study on the mean velocity characteristics in turbulent pipe flow. *Journal of Fluid Mechanics, 608*, 81-112.

Yao, J., & Fairweather, M. (2010). Inertial particle resuspension in a turbulent, square duct flow. *Physics of Fluids, 22*, 033303.

Yao, J., & Fairweather, M. (2012). Particle deposition in turbulent duct flows. *Chemical Engineering Science, 84*, 781-800.

Yao, J., Li, J., & Zhao, Y. (2020). Investigation of granular dispersion in turbulent pipe flows with electrostatic effect. *Advanced Powder Technology, 31*, 1543-1555.

Zhao, Y., Tang, C., Yao, J., Zeng, Z., & Dong, S. (2020). Investigation of erosion behavior of 304 stainless steel under solid–liquid jet flow impinging at 30°. *Petroleum Science, 17*, 1135-1150.

Zhao, Y., Wang, Y., Yao, J., & Fairweather, M. (2018). Reynolds number dependence of particle resuspension in turbulent duct flows. *Chemical Engineering Science, 187*, 33-51.

Figures

Figure 1

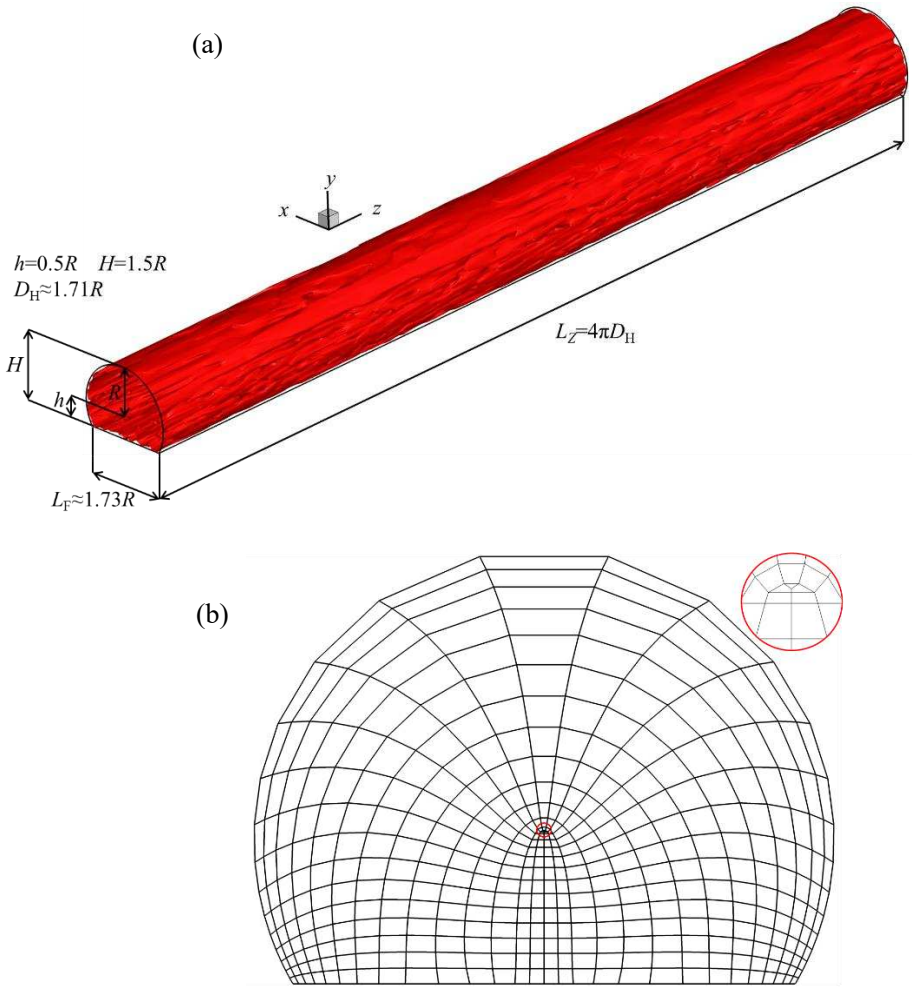

Fig. 1 (a) Flow configuration and instantaneous isosurface of streamwise velocity w=0.8U_b at Re_b=40,000; and (b) grid structure generated by solving Poisson equation. Upper right of (b) is enlarged view of central portion of grid.

Figure 2

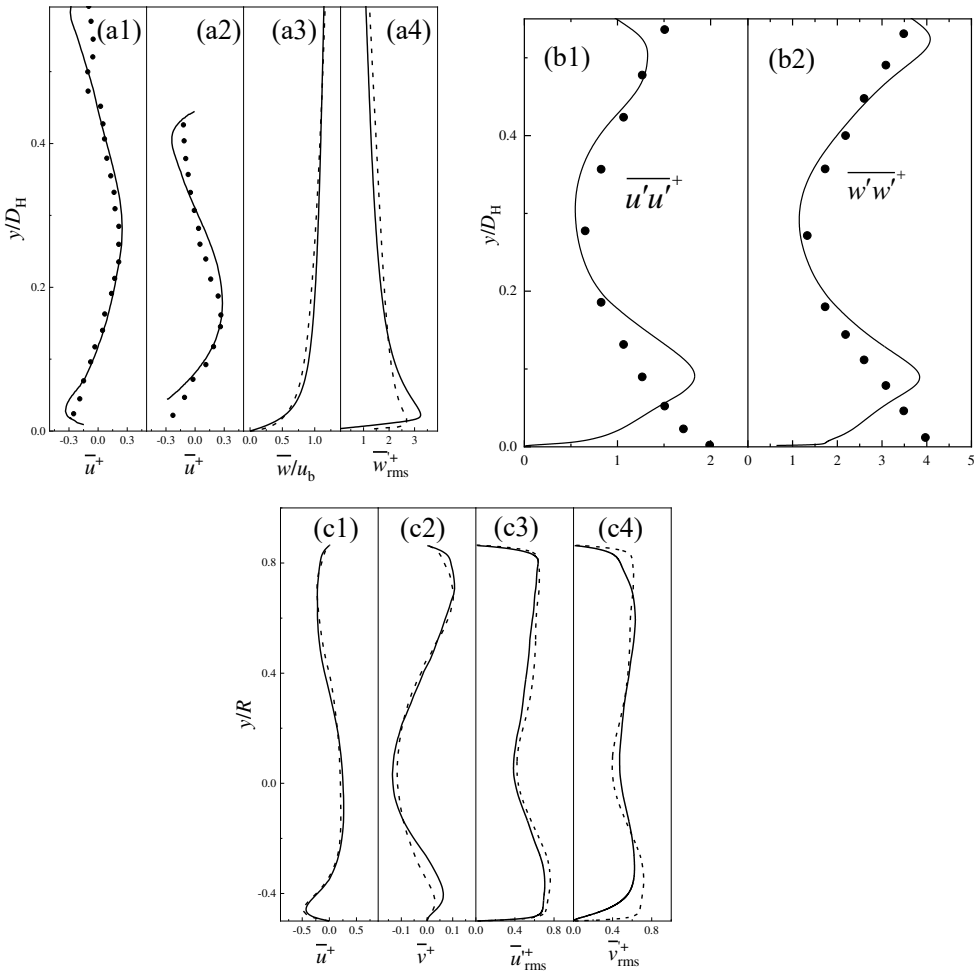

Fig. 2 Fluid spanwise mean velocity u normalized by u_τ along (a1) $x = 0.5R$ and (a2) $x = 0.7R$ in sedimentary pipe flow ($H = 0.7R$), and (a3) mean streamwise velocity, and (a4) streamwise velocity fluctuations along radius in full pipe flow ($H = 2R$) (— present simulation, ● experimental data (Larsson et al., 2011), --- DNS (Wu and Moin, 2008)); (b1)-(b2) velocity fluctuations normalized by u_τ along $x = 0.5R$ (— present simulation, ● experimental data (Larsson et al., 2011)); and (c1)-(c4) mean and fluctuating velocities along $x = 0.5R$ in present (H=1.5R) flat sedimentary pipe flow using 1.08 $\times 10^6$ nodes (---) and 1.90$\times 10^6$ nodes (—).

Figure 3

(a)

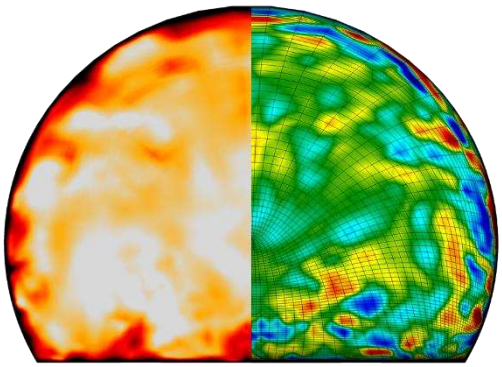

(b)

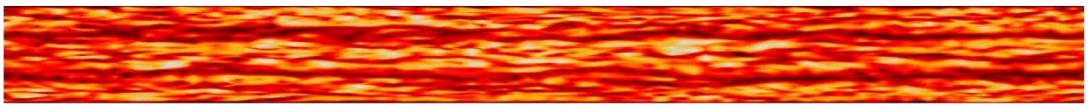

Fig. 3 (a) Contours of instantaneous streamwise velocity w (left) and instantaneous streamwise vorticity ω_z (right) in a cross-section of the sedimentary pipe flow, normalized by bulk flow velocity. ω_z (scaled by u_b and D_H) is plotted in the range of (−7, 7) with dark blue denoting minimum and dark red denoting maximum values. The contours of w vary from 0 (black) to 1.14 (white). A cross-sectional view of a half-section of the computational mesh is shown; and (b) top view of instantaneous streamwise velocity (at $(y+h)/D_H = 0.01$, $\approx 20\ y^+$ from lower wall) in pipe flow. Flow direction is from left to right and contours of w vary from 0 (black) to 1.14 (white).

Figure 4

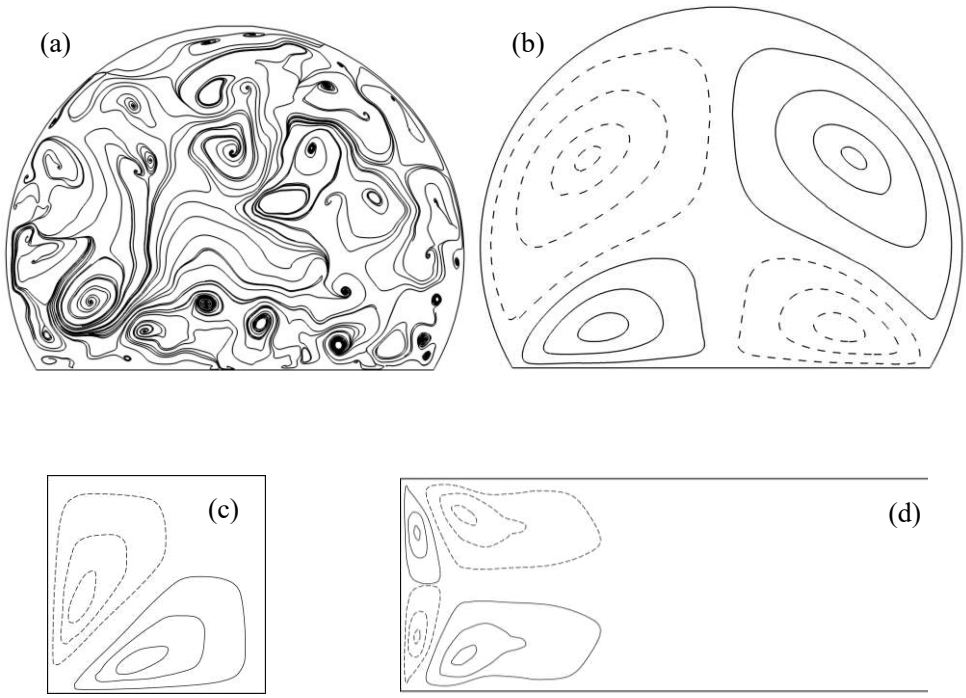

Fig. 4 (a) Instantaneous and (b) averaged cross-stream streamlines in sedimentary pipe flow; (c) in a quarter of a square duct (Wang et al., 2019); and (d) in half of a rectangular duct with aspect ratio 7 (Vinuesa et al., 2016). Solid line indicates counter-clockwise rotation and dashed line indicates clockwise rotation in (b), (c) and (d).

Figure 5

(a)

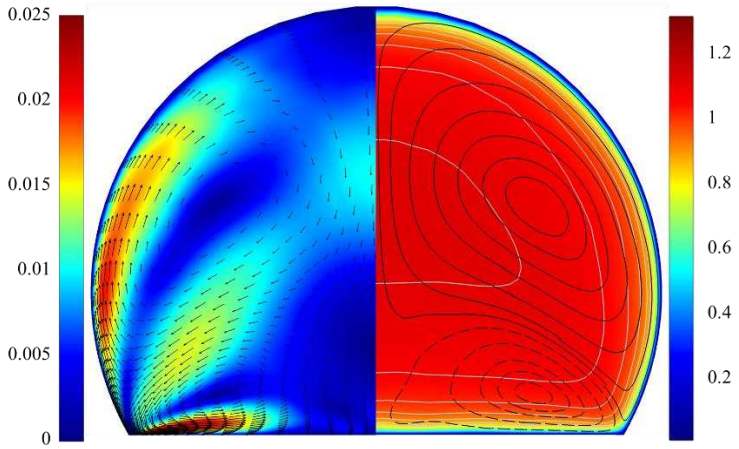

(b)

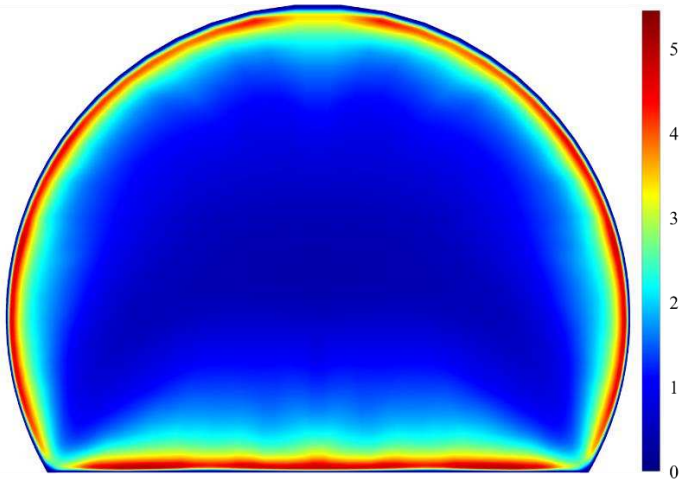

Fig. 5 (a) Contours of magnitude of mean flow velocity ($\sqrt{\overline{u}^2+\overline{v}^2}$) with velocity vectors (left) and of streamwise component of mean flow velocity with isocontours of $\overline{w}$ ($\in$[0.5, 1.1]/0.1) in grey (right). Isocontours of cross-flow stream function projected on top where dashed lines represent negative values of ψ ((ψ_{min}, ψ_{max})×10^3 for sedimentary pipe flow is (−2, 2)). Velocity and length scales used in (a) are bulk velocity u_b and hydraulic diameter D_H, respectively; and (b) contours of turbulence kinetic energy of fluid phase normalized by flow friction velocity u_τ^2.

Figure 6

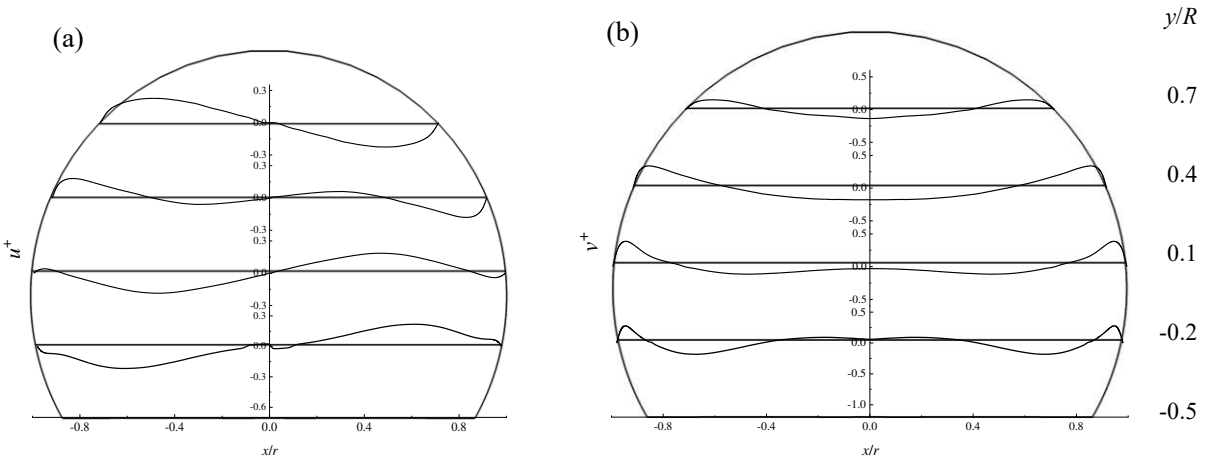

Fig. 6 (a) Spanwise velocity $\overline{u}^+$; and (b) vertical velocity $\overline{v}^+$ normalized by u_τ at y/R = -0.2, 0.1, 0.4, 0.7.

Figure 7

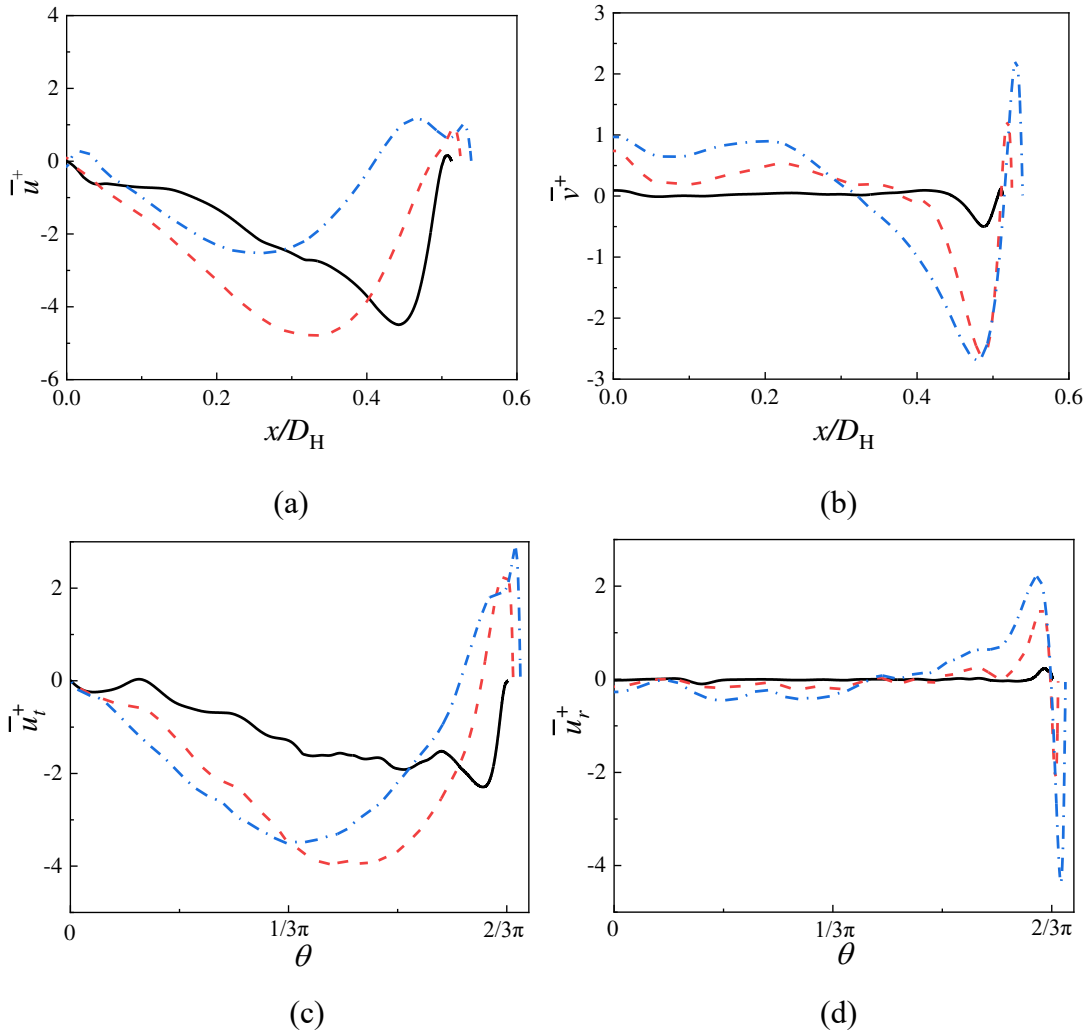

Fig. 7 (a) $\overline{u}^+$ and (b) $\overline{v}^+$ profiles at $(y+h)^+=$ ——10, - - - -50, -·-·-100; and (c) $\overline{u}_t^+$ and (d) $\overline{u}_r^+$ profiles at $(R-\sqrt{x^2+y^2})^+=$ ——10, - - - -50, -·-·-100. $\overline{u}_t^+$ is circumferential velocity (parallel to upper wall); $\overline{u}_r^+$ is radial velocity perpendicular to upper wall; corners: $\theta=\pm 2/3\pi$; top $\theta=0$. Velocity scale is normalized by u_τ.

Figure 8

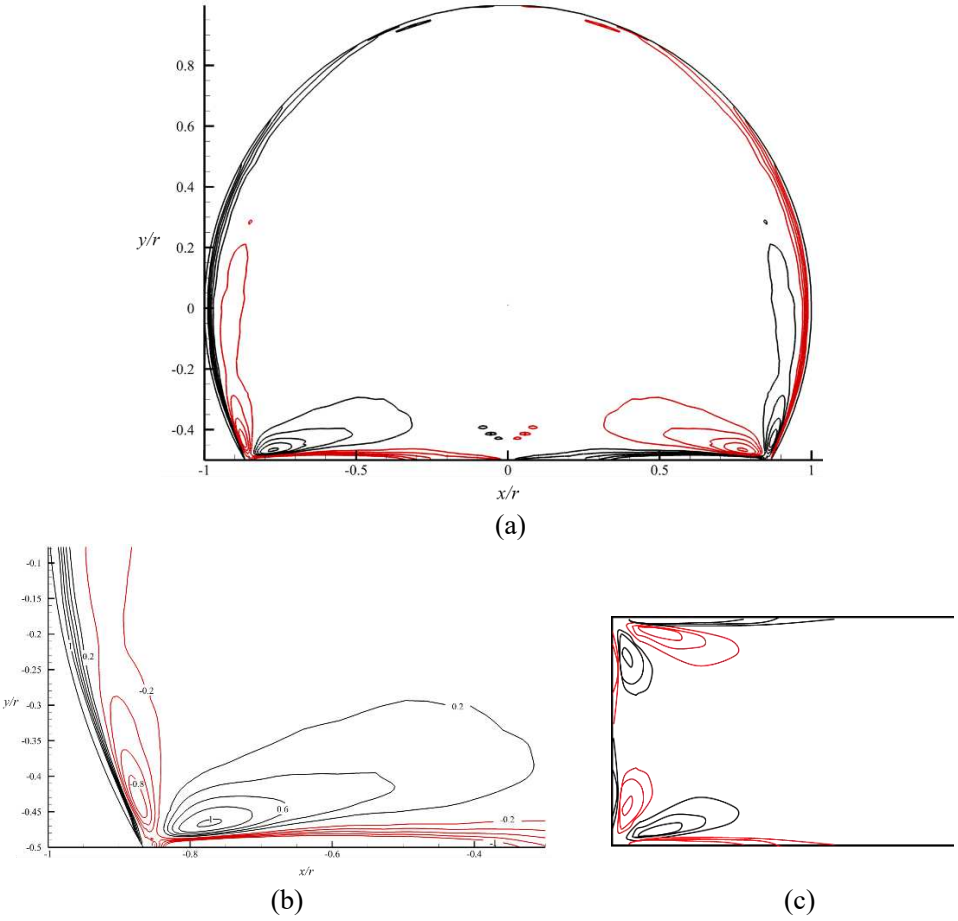

Fig. 8 (a) Contours of mean streamwise vorticity scaled by u_b and D_H in sedimentary pipe flow; (b) an enlarged view of (a) in the pipe corner; and (c) contours of mean streamwise vorticity in a rectangular duct with aspect ratio 3 (Vinuesa et al., 2016).

Figure 9

Fig. 9 Instantaneous isosurfaces of streamwise velocity for (a) $w = 1.15u_b$; and (b) $w = 1.2u_b$.

Figure 10

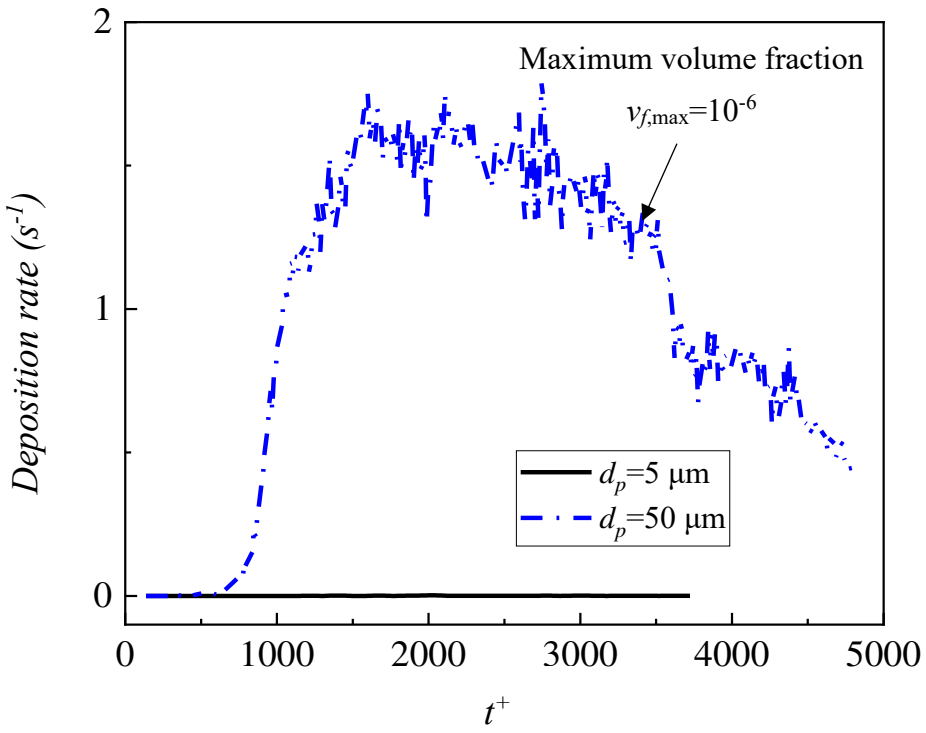

Fig. 10 Overall deposition rate of particles in period t^+ = 0-3700 for d_p = 5μm and t^+ = 0-4800 for d_p = 50μm particles, where time scale is normalized by t^*.

Figure 11

(a)

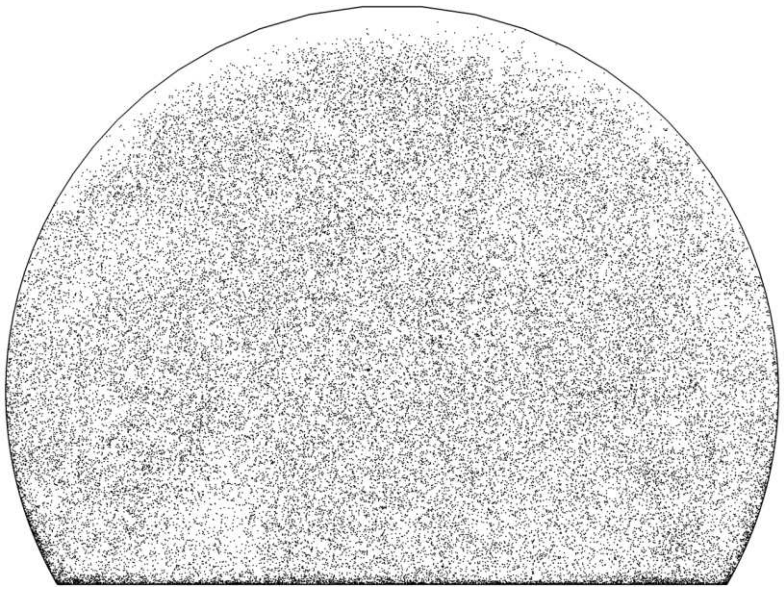

(b)

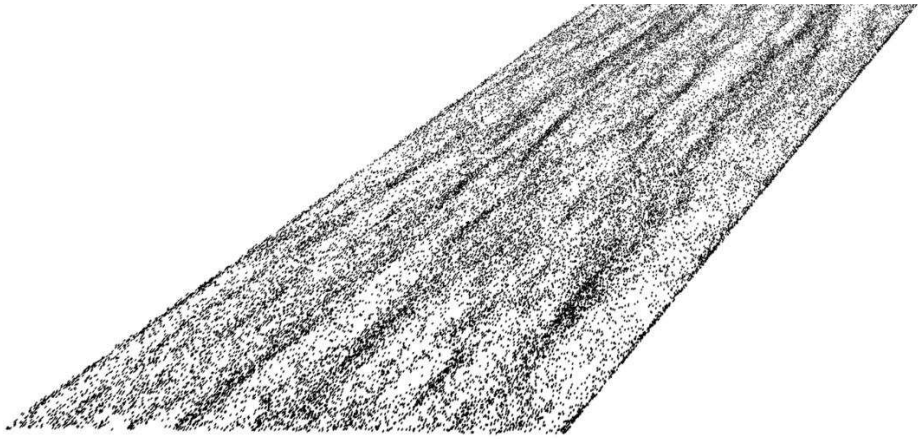

Fig. 11 (a) Projected instantaneous view for 50μm particles distributed in the cross-section of sedimentary pipe; and (b) a cut-away view of 50μm particles distributed near floor with $(y+h)^+ \approx 10$. $t^+ = 800$ normalized by t^*.

Figure 12

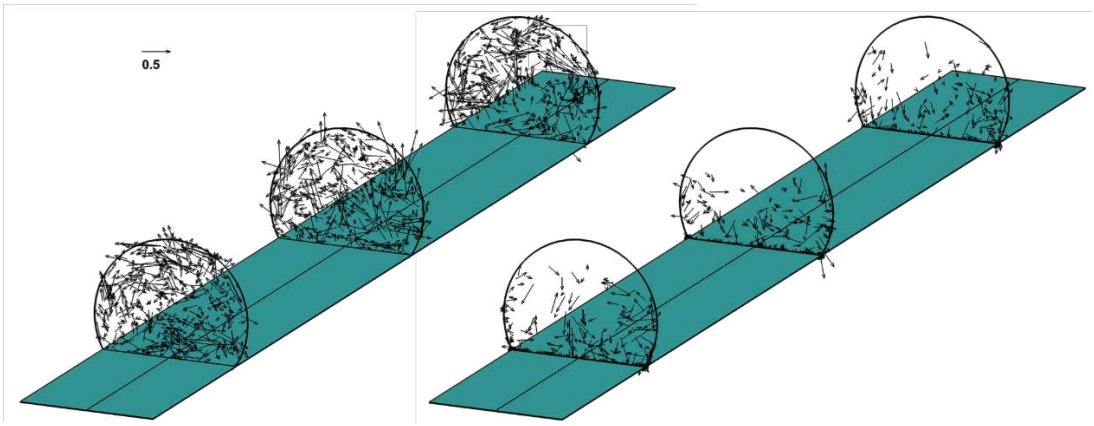

(a) (b)

Fig. 12 Instantaneous particle distribution in plane z= 1/6L_z, 1/2L_z, 5/6L_z at t^+=3700 normalized by t^*. The arrow indicates the in-plane velocity of the particles. (a) d_p=5μm; (b) d_p=50μm.

Figure 13

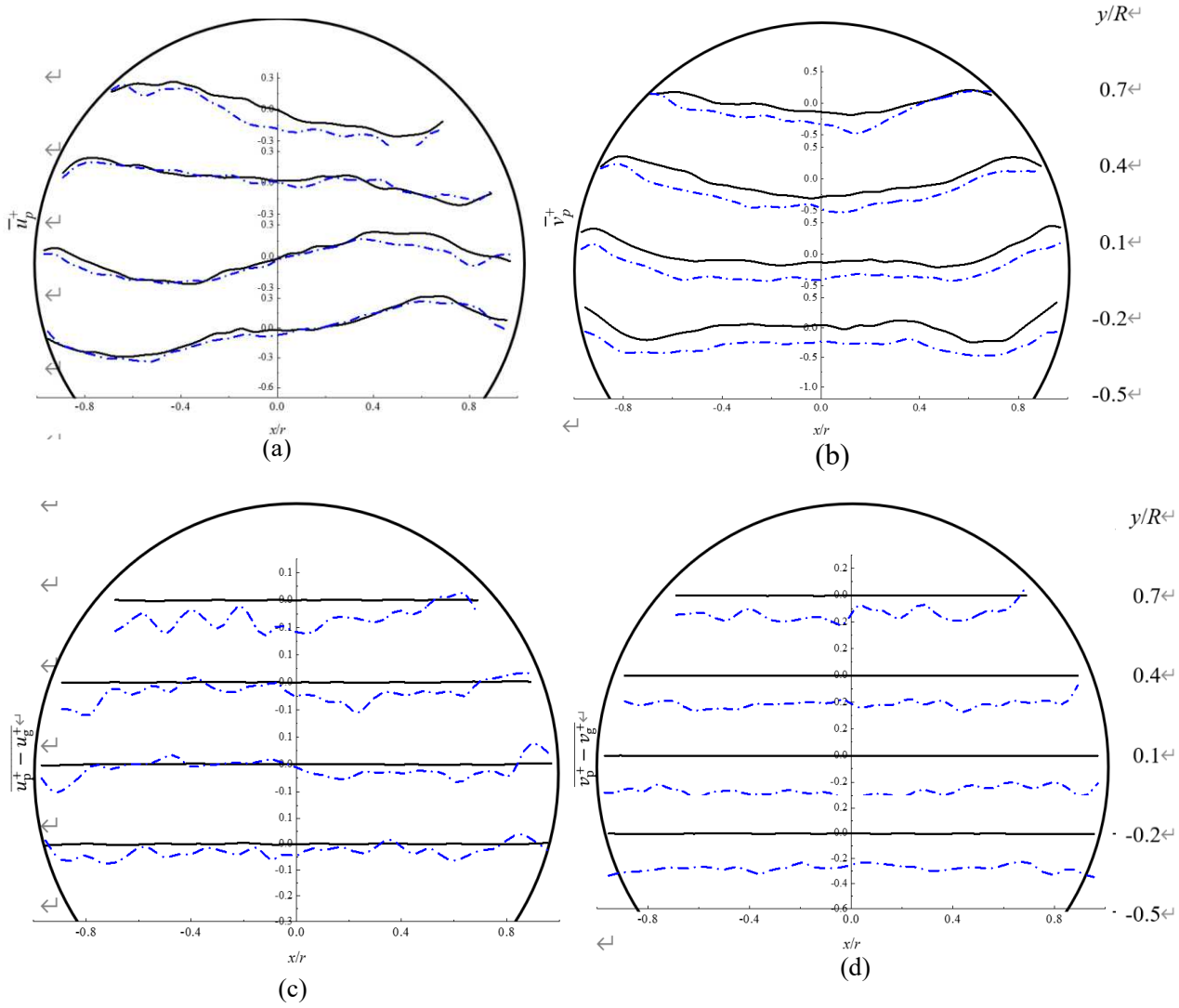

Fig. 13 Time-averaged (t^+=1500-3000, normalized by t^*) particle velocity in (a) spanwise and (b) vertical directions, and particle slip velocity in (c) spanwise and (d) vertical directions, at y/R = -0.2, 0.1, 0.4, 0.7. —— 5μm and - · - · - 50μm. Velocity scale is normalized by u_τ.

Figure 14

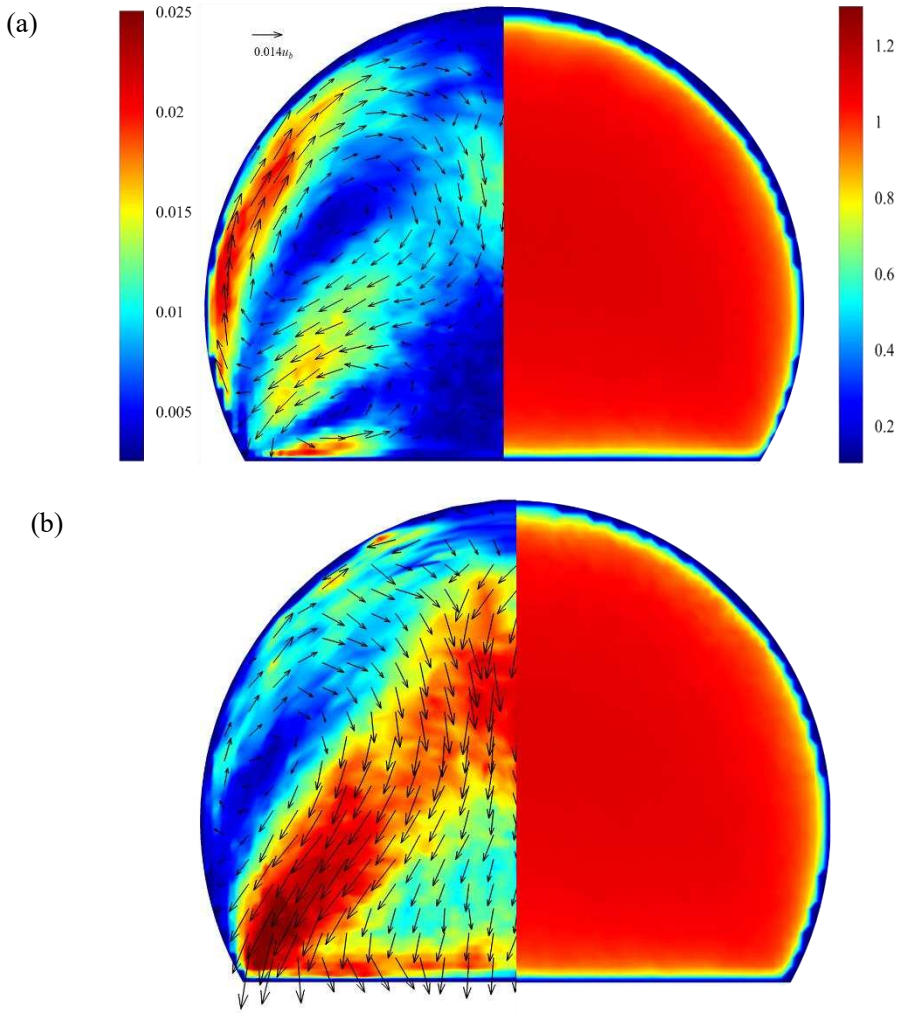

Fig. 14 Contours of time-averaged (t^+ = 1500-3000, normalized by t^*) particle velocity with velocity vectors of particle motion (left) and contours of mean particle velocity in streamwise direction (right). (a) $d_p = 5\mu m$; and (b) $d_p = 50\mu m$. Velocity and length scales used are bulk velocity u_b and hydraulic diameter D_H, respectively.

Figure 15

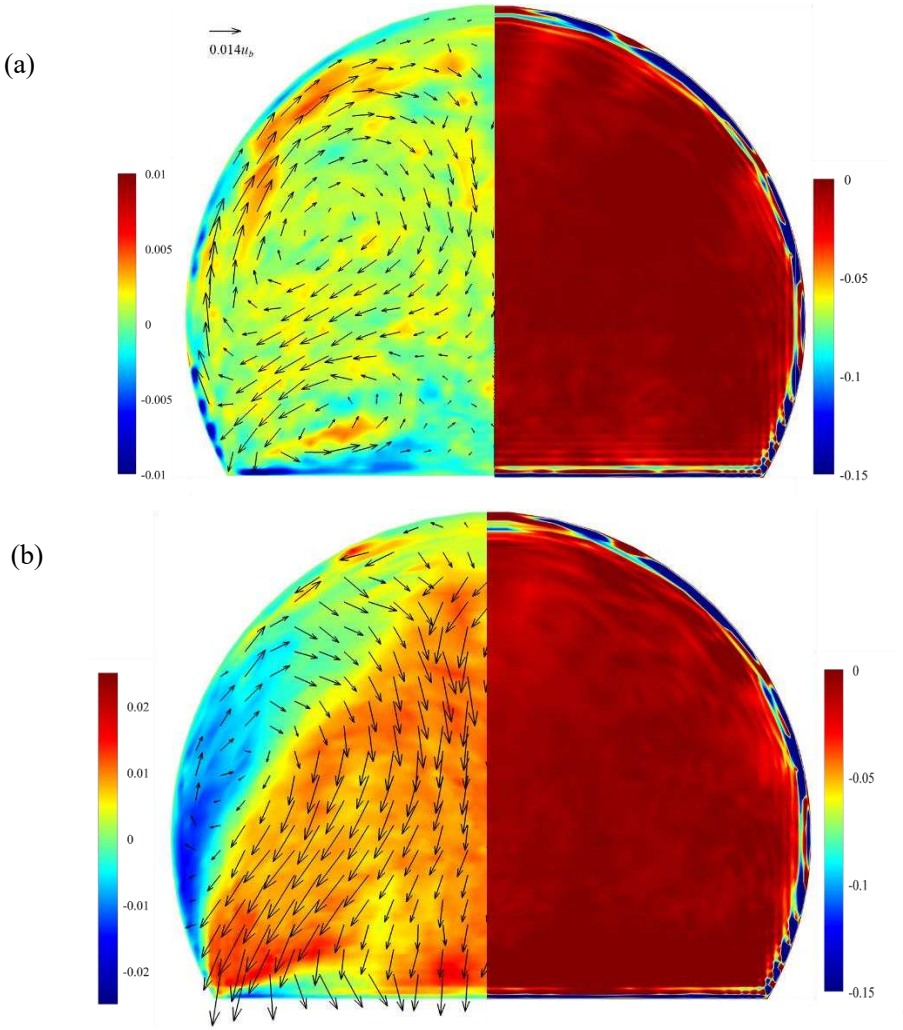

Fig. 15 Contours of difference between time-averaged (t^+=1500-3000, normalized by t^*) particle velocity and local flow velocity with velocity vectors of particle motion (left) and contours of difference between time-averaged particle velocity and local flow velocity in streamwise direction (right). (a) $d_p = 5\mu m$; and (b) $d_p = 50\mu m$. Velocity used is bulk velocity u_b and length scale is hydraulic diameter D_H.

Figure 16

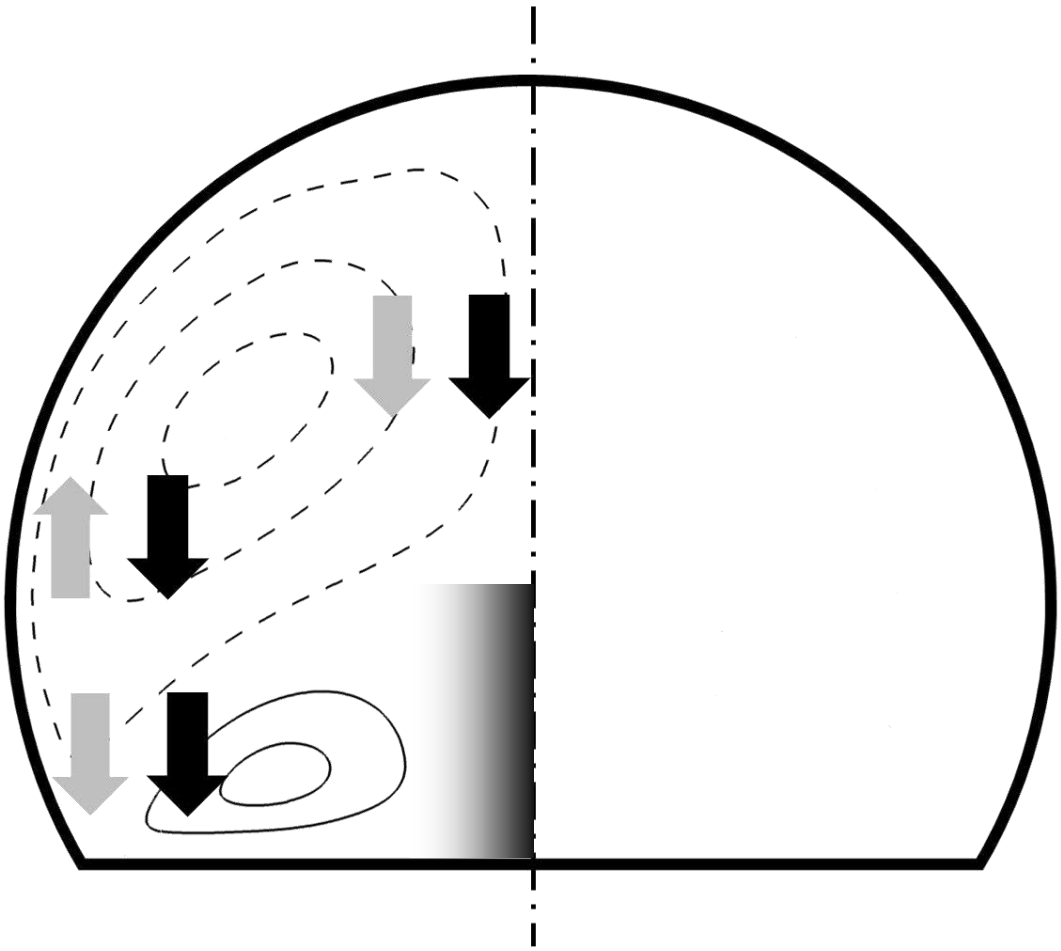

Fig. 16 Schematic illustration of secondary flow in sedimentary pipe. Light grey arrows represents flow motion in *y*-direction while black arrows show downward motion of particles caused by effect of gravity.

Figure 17

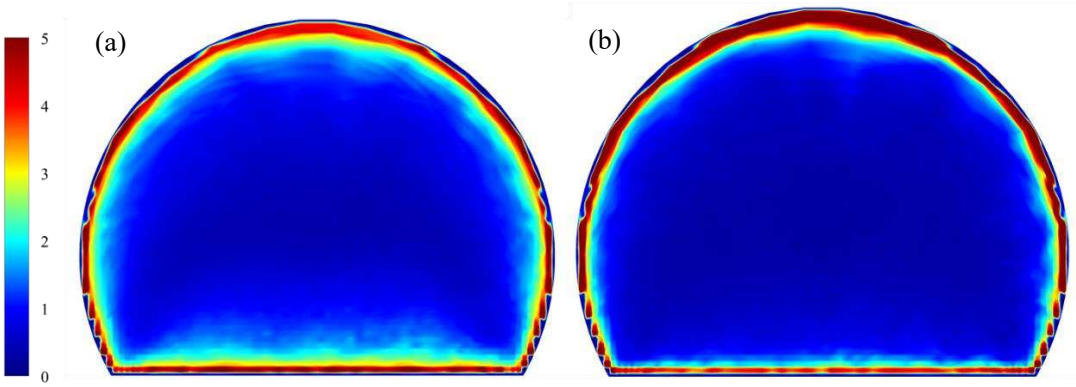

Fig. 17 Contours of time-averaged (t^+=1500-3000, normalized by t^*) turbulence kinetic energy of particles normalized by flow friction velocity u_τ^2. (a) $d_p = 5\mu m$; and (b) $d_p = 50\mu m$.

Figure 18

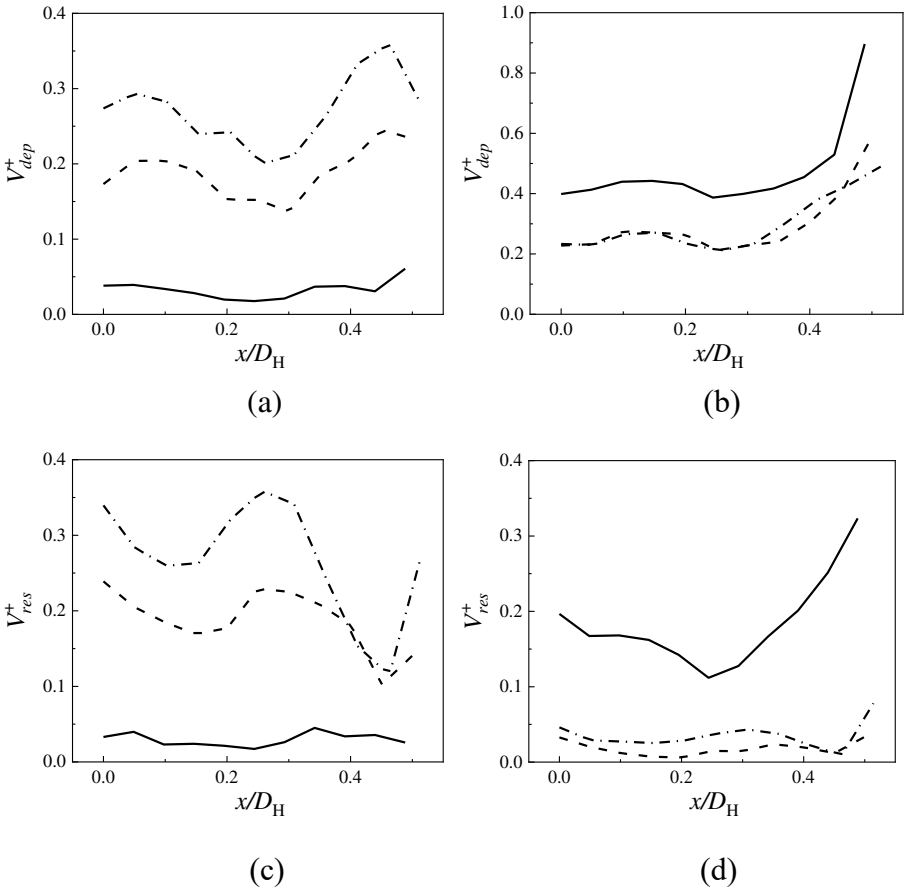

Fig. 18 (a) and (b) Time-averaged (t^+=1500-3000, normalized by t^*) deposition rate $V_{dep}{}^+$ profiles; and (c) and (d) resuspension rate $V_{res}{}^+$ profiles at $(y+h)^+$ = ——— 10, - - - - - 50, _ . _ . _ . _ 100. (a) and (c) $d_p = 5\mu m$; and (b) and (d) d_p=50μm. Rate and length scales are normalized by u_τ and l*, respectively.

Figure 19

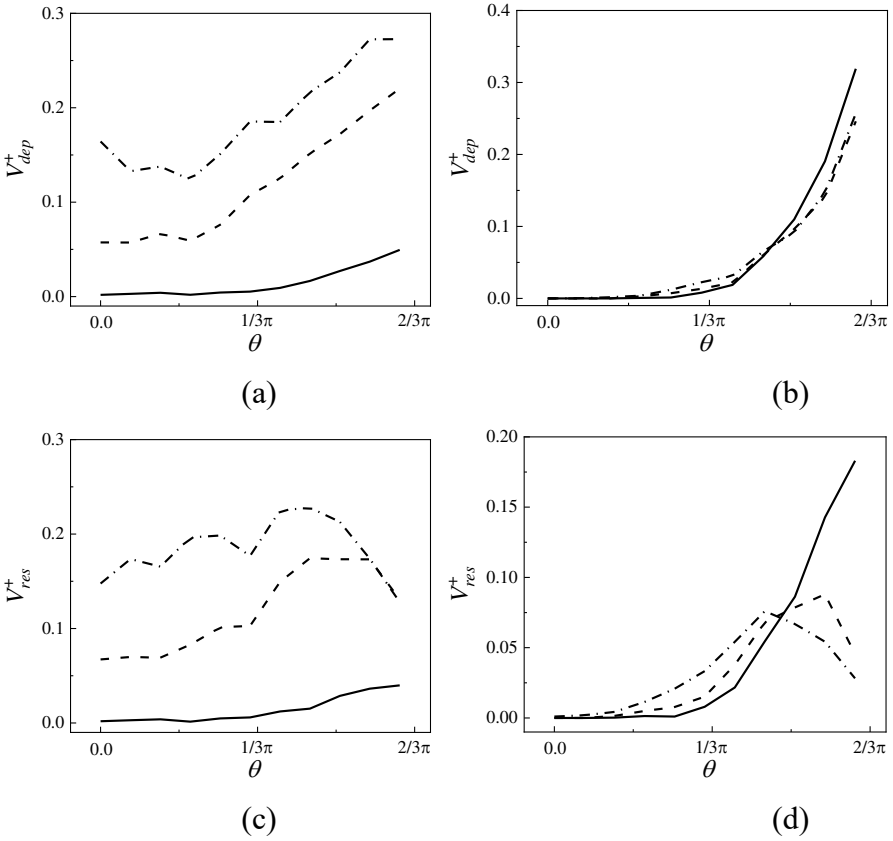

Fig. 19 (a) and (b) Time-averaged (t^+=1500-3000, normalized by t^*) deposition rate $V_{dep}{}^+$ profiles; and (c) and (d) resuspension rate $V_{res}{}^+$ profiles at $(R-\sqrt{x^2+y^2})^+$ = ——— 10, - - - - - 50, _._._._ 100. θ is $\pm 2/3\pi$ at corners, and 0 at top. (a) and (c) d_p = 5μm; and (b) and (d) d_p = 50μm. Rate and length scales are normalized by u_τ and l^*, respectively.